Step-wise evolution of azole resistance through copy number variation followed by *KSR1* loss of heterozygosity in *Candida albicans*.

Pétra Vande Zande[1], Cécile Gautier[2], Nora Kawar[3], Corinne Maufrais[2,4], Katura Metzner[1], Elizabeth Wash[1], Annette Beach[1], Ryan Bracken[1], Eli Isael Maciel[2], Caroline Mota Fernandes[5], Norma V. Solis[8], Maurizio Del Poeta[5,6,7], Scott G. Filler [8,9], Judith Berman[3], Iuliana V. Ene[2], Anna Selmecki[1]

[1]Department of Microbiology and Immunology, University of Minnesota, Minneapolis, MN, USA

[2]Institut Pasteur, Université Paris Cité, Fungal Heterogeneity Group, Paris, France

[3]Shmunis School of Biotechnology and Cancer Research, George S. Wise Faculty of Life Sciences, Tel Aviv University, Ramat Aviv, Israel

[4]Institut Pasteur Bioinformatic Hub, Université Paris Cité, Paris, France

[5]Department of Microbiology and Immunology, Stony Brook University, Stony Brook, New York, USA

[6]Division of Infectious Diseases, School of Medicine, Stony Brook University, Stony Brook, New York, USA

[7]Veterans Administration Medical Center, Northport, New York, USA

[8]Division of Infectious Diseases, Lundquist Institute for Biomedical Innovation at Harbor UCLA Medical Center, Torrance, CA, USA

[9]David Geffen School of Medicine at UCLA, Los Angeles, CA, USA

* Corresponding author

Email: selmecki@umn.edu (AS)

Abstract

Antimicrobial drug resistance poses a global health threat, requiring a deeper understanding of the evolutionary processes that lead to its emergence in pathogens. Complex evolutionary dynamics involve multiple mutations that can result in cooperative or competitive (clonal interference) effects. *Candida albicans*, a major fungal pathogen, displays high rates of copy number variation (CNV) and loss of heterozygosity (LOH). CNV and LOH events involve large numbers of genes and could synergize during evolutionary adaptation. Understanding the contributions of CNV and LOH to antifungal drug adaptation is challenging, especially in the context of whole-population genome sequencing. Here, we document the sequential evolution of fluconazole tolerance and then resistance in a *C. albicans* isolate involving an initial CNV on chromosome 4, followed by an LOH on chromosome R that involves *KSR1*. Similar LOH events involving *KSR1,* which encodes a reductase involved in sphingolipid biosynthesis, were also detected in independently evolved fluconazole resistant isolates. We dissect the specific *KSR1* codons that affect fluconazole resistance and tolerance. The combination of the chromosome 4 CNV and *KSR1* LOH results in a >500-fold increase in azole resistance, illustrating a compelling example of rapid, yet step-wise, interplay between CNV and LOH in drug resistance evolution.

Introduction

The evolutionary processes that lead to the emergence of antimicrobial drug resistance in pathogens pose a global health threat. Understanding the evolution of resistance is complicated by the fact that multiple mutations often arise in the same population and either compete with each other (clonal interference) or co-occur in the same genetic background, thereby contributing to resistance either additively or epistatically [1–4]. *Candida albicans,* common commensal and pathogen of humans, undergoes high rates of copy number variation (CNV)

and loss of heterozygosity (LOH) [5–8], which often affect many genes and can contribute to evolutionary adaptation. However, CNV and LOH can be difficult to identify in populations of cells via whole genome sequencing. Therefore, the dynamics by which CNV and LOH drive adaptation to drug stress, how the two types of mutations interact, and the mechanisms by which they influence drug resistance are not fully understood.

Ergosterol, the fungal analog of cholesterol, is a key regulator of membrane fluidity. Two of the three major classes of antifungal drugs target ergosterol directly or indirectly. Azole drugs target lanosterol 14-alpha demethylase, a cytochrome P450 that catalyzes a key step in the ergosterol biosynthesis pathway, which is encoded by the gene *ERG11* in *C. albicans*. Mutations that occur in *ERG11* itself [4,9,10], those which affect its expression level [11–14], or mutations in other genes in the ergosterol biosynthesis pathway such as *ERG3* [15–17] can confer azole drug resistance to *C. albicans* isolates and other *Candida* species. However, the most prevalent resistance mechanisms affect the expression or activity of drug efflux pumps that remove azole drugs from the cell, thereby reducing Erg11p inhibition and restoring some level of ergosterol biosynthesis [1,3,18–21]. Together with sphingolipids, ergosterol also contributes to lipid raft formation and membrane polarization. The polarization of the lipid membrane is necessary for filamentation [22], a key virulence trait, and lipid rafts are important for the proper localization and activation of membrane-associated proteins including efflux pumps [23]. Thus, azole resistance and tolerance are also influenced by sphingolipid biosynthesis [21,24].

Azole tolerance, in contrast to resistance, is defined as slower persistent growth that is independent of drug concentration. Resistance is measured in the clinic as the drug concentration that reduces growth by 50% or more at 24 h (Minimum Inhibitory Concentration, MIC_{50}) [25]; tolerance is measured as the relative growth in supra-MIC concentrations of drug at 48 h (supra-MIC growth, SMG) [21,26]. While tolerance relies upon the robust function of many

stress response pathways [26], and high tolerance has been associated with clinical persistence during treatment [26–29], we do not yet understand how mutations conferring high tolerance impact treatment, and whether they might precede or be connected to the acquisition of drug resistance.

Multiple mechanisms could link sphingolipid biosynthesis (S1 Fig) to azole resistance and/or tolerance [24]. Null mutations in two genes, *FEN1* and *FEN12*, which catalyze sphingolipid precursor formation, increase azole resistance and tolerance by upregulating sphingolipid biosynthesis genes and increasing complex sphingolipid levels [30]. Overexpression of *LCB4*, a putative sphingosine kinase (S1 Fig), affects fluconazole tolerance [31], while a heterozygous deletion of *LCB4* increases azole susceptibility [32]. Azole susceptibility in *LCB4/lcb4* mutants can be ameliorated by the addition of the metabolic intermediate phytosphingosine-1-P (PhytoSph-1-P), which leads to upregulation of drug efflux pumps [32]. In addition, chemical inhibitors of sphingolipid synthesis including aureobasidin A, which targets *AUR1*, [33,34]; NPD827, which likely targets *LCB1/LCB2* [35]; MMV688766 [36]; and myriocin, which inhibits 3-ketosphinganine formation [34], all synergize with azoles by disrupting the localization or activation of drug efflux pumps. 3-ketosphinganine, which is inhibited by myriocin, is reduced by the 3-ketosphinganine reductase encoded by *KSR1* (S1 Fig). Despite its importance in the sphingolipid pathway [37], *KSR1* has not been previously connected to resistance. However, a *ksr1*Δ*/ksr1*Δ null mutant generated in a lab strain increased the fluconazole MIC_{50} by 2-fold [37], providing initial evidence that changes to *KSR1* function could influence azole responses.

The heterozygosity of the *C. albicans* diploid genome serves as a rich source of recessive variants that can be revealed rapidly via LOH [8,38,39]. The *C. albicans* reference genome from isolate SC5314 contains almost 200 heterozygous nonsense alleles that encode early stop codons [39]; such alleles might limit the selection of LOH events if they are recessive lethal [40].

Yet heterozygous recessive alleles can also be advantagous when homozygosed via LOH events [41–43]. For example, homozygosis of a hyperactive allele of the efflux pump regulator Tac1p can confer high levels of azole resistance [19]. LOH in *C. albicans* frequently affects long portions of chromosome arms, encompassing thousands of heterozygous positions [44,45], thereby making it difficult to pinpoint the specific genes and nucleotides by which such events affect antifungal drug responses. As a result, despite their prevalence, the mechanisms by which most LOH events affect phenotypes remain unknown.

CNV is another important class of mutations frequently found in *C. albicans* strains that evolve under stress. Both whole-chromosome and segmental aneuploidy are associated with increased resistance and/or tolerance to antifungal drugs in clinical isolates and in laboratory evolution experiments [46–48]. In some cases, the mechanisms causing increased resistance via CNV have been identified. For example, amplification of the left arm of chromosome (Chr) 5 occurs via an isochromosome structure (i(5L)) that provides two additional copies of the fluconazole (FLC) target *ERG11* and of a transcriptional activator of drug efflux pumps, *TAC1*; the extra copies of these two genes largely explains the drug resistance in strains carrying the i(5L) karyotype [12,49]. While the specific mechanisms of resistance have not been elucidated for most CNVs, the recurrent association of increased resistance or tolerance with specific CNVs suggests that specific genes within these amplified regions are responsible for increased resistance [46,47,50,51]. As with LOH, identifying the mechanisms of drug resistance is complicated by the large number (often hundreds) of genes amplified within a given CNV, any of which could potentially contribute to resistance via different mechanisms.

Here, we describe the step-wise evolution of an azole resistant isolate of *C. albicans* via an initial CNV on Chr4, followed by a small LOH on ChrR. These two events contribute additively to drug resistance and result in a final evolved MIC_{50} of >256 µg/mL FLC. Furthermore, we identify

NCP1, a gene within the Chr4 CNV, whose overexpression results in a 2-fold increase in MIC_{50}. We also localize the specific nucleotides affected by the LOH on ChrR to the *KSR1* coding sequence and show that they are important for increased resistance and tolerance. Combining the LOH in *KSR1* with the Chr4 CNV increases resistance by >500-fold, providing a powerful example of rapid step-wise evolution of drug resistance via different mechanisms. Furthermore, in the reference isolate SC5314, *KSR1* contains a heterozygous nucleotide that encodes an early stop codon; this nonsense allele predicts a truncated protein that lacks a membrane localization domain. Remarkably, four independent LOH events that each affect residues in *KSR1* do not generate homozygous early stop codons. This highlights the power of LOH to recombine heterozygous variants and to de-couple linked variants in *C. albicans*.

Results

Step-wise acquisition of increased resistance during adaptation to fluconazole

We recently identified a lineage (AMS4058) in an evolution experiment in which the drug sensitive progenitor strain SC5314 acquired FLC resistance after 10 passages in 1 μg/mL FLC, resulting in an increase in MIC_{50} from 0.5 μg/mL to >256 μg/mL FLC [47]. The AMS4058 lineage also had reduced filamentation *in vitro* and decreased virulence in a mouse model of disseminated candidiasis (S2 Fig A,B). To understand the dynamics of adaptation in lineage AMS4058, we measured the MIC_{50} at each of the 10 passages. The MIC_{50} increased 2-fold after passage 1 and after passage 3; and increased dramatically to >256 μg/mL FLC after passage 4 (Fig 1A). We also measured FLC tolerance after each passage (supra-MIC growth, SMG, see Methods) [21,26]. SMG increased dramatically after the first passage and steadily decreased in passages 2 and 3 (Fig 1B). We hypothesized that variants conferring large increases in

tolerance were dominant early in the evolution experiment (passages 1 to 3), whereas variants conferring high levels of resistance arose around passage 4 and continued to increase in frequency in all subsequent passages.

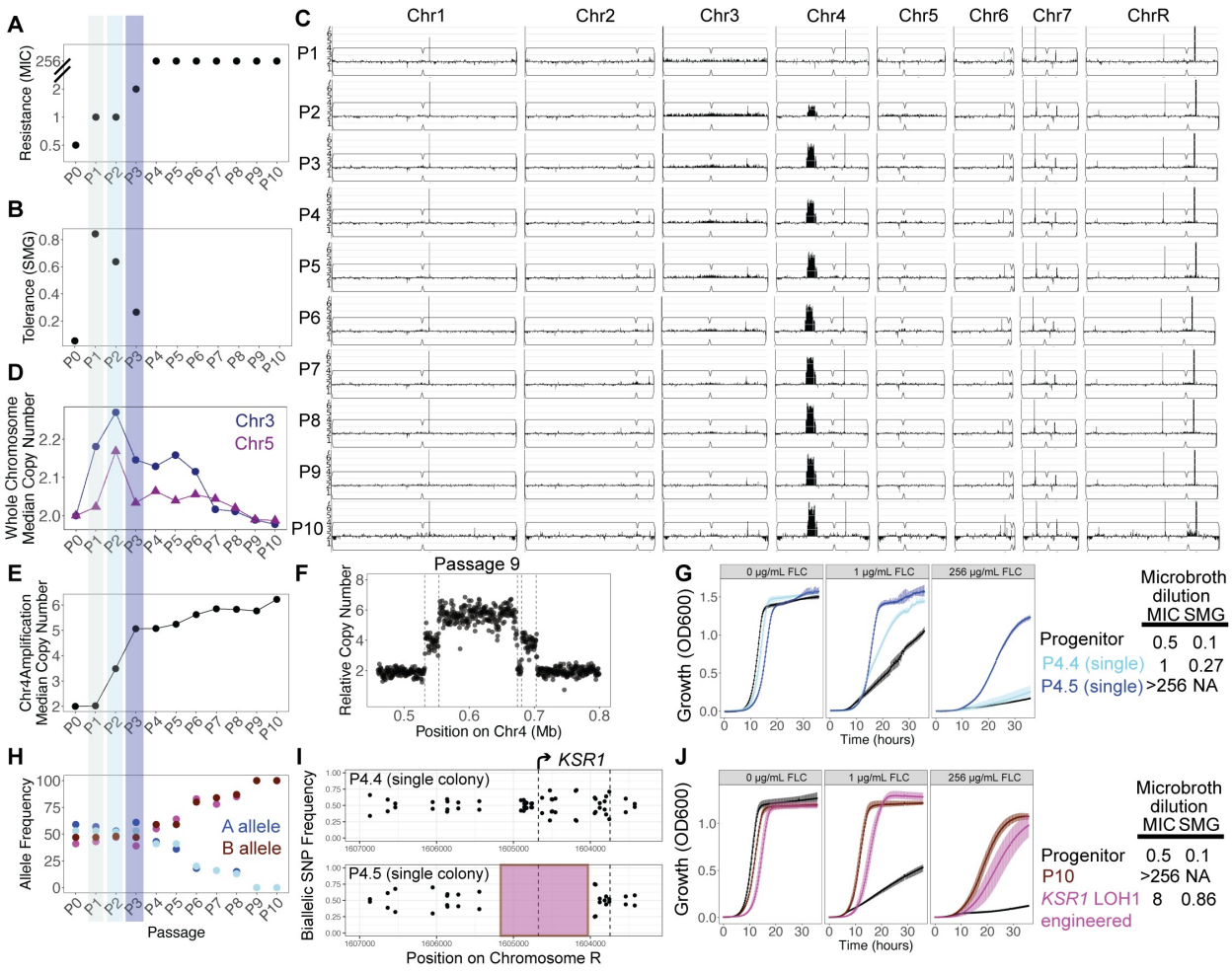

Fig 1. Step-wise evolution of drug resistance via CNV and LOH. (A) MIC_{50}, defined as the drug concentration at which growth is inhibited by >50%, is plotted on the y-axis for each passage of the evolution experiment. (B) SMG, defined as the average growth in drug concentrations greater than the MIC_{50}, is plotted on the y-axis for each passage of the evolution experiment. (C) Read depth from whole genome sequencing of the entire population for each passage of the evolution experiment is plotted according to genomic position and normalized to the average read depth for the entire genome. (D) Median copy number, calculated from read

depth relative to the entire genome, for whole chromosomes with variation in copy number (Chr3 and Chr5) is plotted on the y-axis for the entire population at each passage of the evolution experiment. (E) Median copy number of the central amplified portion of Chr4, calculated from read depth in the entire passaged population relative to the rest of the genome, is plotted on the y-axis at each passage of the evolution experiment and connected by line segments. (F) Relative copy number for the entire population at passage 9 at the region containing a CNV, calculated from the relative average read depth, is plotted on the y-axis according to the position on Chr4 on the x-axis. Each point represents the average read depth of a 500 bp window. Dashed lines show the location of repeat sequences in the *C. albicans* genome [50]. (G) OD_{600} values for liquid culture growth assays are plotted over time for the wild-type progenitor (black), a single colony containing the Chr4 amplification without LOH at *KSR1* (P4.4 single colony, light blue), and a single colony containing the Chr4 amplification with the LOH at *KSR1* (P4.5 single colony, dark blue). Growth in rich media, 1 µg/mL FLC, and 256 µg/mL FLC are shown. Error bars are standard errors for three replicates. Points are averages. A table to the right shows average MIC_{50} and SMG values for the listed strains. (H) Allele frequencies for 2 single nucleotide variants at *KSR1* amino acid positions 189 and 192 are plotted for each passage of the evolution experiment. Reference “A” alleles are shown in cyan, and reference “B” alleles are shown in magenta. (I) Biallelic single nucleotide polymorphism (SNP) frequencies are plotted across the *KSR1* locus on chromosome R for two single colonies isolated from passage 4, with MIC_{50} = 1 (P4.4, top) and MIC_{50} >256 µg/mL FLC (P4.5, bottom). The absence of biallelic SNPs in P4.5 indicates a loss of heterozygosity highlighted by the pink-shaded region. (J) OD_{600} values for liquid culture growth assays are plotted over time for the wild-type progenitor (black), the P10 evolved population (red), and a strain engineered to contain the LOH at *KSR1* (pink). Growth in rich media with 0 µg/mL, 1 µg/mL, or 256 µg/mL FLC are shown. Error bars are standard errors for three replicates. Points are averages. A table to the right shows MIC_{50} and SMG values for the listed strains.

Aneuploidy and copy number variation arise early and yield moderate increases in fluconazole tolerance and resistance

To identify the genetic changes associated with increases in drug tolerance and resistance, we performed population-level whole genome sequencing of each passage of the evolution experiment. We first estimated the population-average copy number of each chromosome by examining sequencing read depth across the genome for all 10 passages. Increases in read depth indicative of copy number variants (CNVs) were present in the population from passage 2 to passage 10 (Fig 1C-E). The median copy number of Chr3 was ~2.18, 2.27, and 2.15 for passages 1, 2, and 3, respectively (Fig 1D), suggesting that ~15-30% of the population was trisomic for Chr3 at these early passages with high tolerance (see Methods). Chr5 also rose to a frequency of ~2.17 by passage 2 (Fig 1D). Chr3 contains several genes encoding efflux pumps and their regulators, such as *CDR1*, *CDR2*, and *MRR1;* and Chr5 contains genes encoding Erg11 (the azole drug target) and efflux pump regulator Tac1. Additional copies of these genes have the potential to contribute to increased resistance and tolerance observed in the early populations of the evolution experiment.

In addition to evidence of aneuploidy, we detected a segmental amplification of Chr4 (Fig 1C,E), consisting of a stair-step structure with two flanking regions (~20-25 kb, A21 Chr4 coordinates ~532000 to ~553000, and ~681000 to ~704500) surrounding a central region with the highest copy number (~100 kb, A21 Chr4 coordinates ~553000 to ~674000) (Fig 1F). Each amplified region was flanked by inverted repeat sequences, consistent with segmental amplifications as previously described (Fig 1F, [50]). Median read depth in the central region increased from a population average relative copy number of 2 in passage 1 to ~3.5 by passage 2, ~5 by passage 3, and then gradually rose to ~6 copies by passage 10 (Fig 1E).

To identify individual genotypes within the passaged populations, we isolated and sequenced 5 single colonies each from passages 2, 3, and 4. Passage 2 included one colony with wild type chromosome copy numbers (euploid), one colony with an LOH of ChrR and duplication of the B homolog, resulting in a ChrR BB genotype, two colonies with monosomy of the right end of ChrR, and one colony with homozygosis of the left arm of Chr4 resulting in an AA genotype (S3 Fig A). For each unique genotype from passage 2 we performed growth curve and microbroth dilution assays and found that the colony with ChrR LOH grew faster than the progenitor strain in all concentrations of FLC, with an MIC_{50} of 2 μg/mL FLC and an SMG of 0.78 (S3 Fig B). In passage 3 we found two distinct genotypes: 2 colonies displayed concurrent trisomy of Chr3 and Chr6 along with LOH encompassing the entirety of ChrR resulting in a ChrR AA genotype; and 3 colonies displayed the Chr4 segmental amplification described above (S3 Fig C). Both genotypes from passage 3 also grew better than the progenitor in FLC, with a slightly elevated MIC_{50} of 1 μg/mL FLC and SMG of 0.25 and 0.3 (S3 Fig D). Thus, early in the evolution experiment, different copy number variants arose and conferred a 2- to 4-fold increase in MIC_{50} and increased tolerance.

The amplified region of Chr4 does not contain genes known to cause increased drug resistance upon overexpression. This region includes ~88 genes, including *NCP1,* which encodes the Erg11p reductase (S4 Fig A). We tested the hypothesis that overexpression of Ncp1p is sufficient to promote growth in 1 μg/mL FLC by engineering strains with *NCP1* under the control of a tet-off promoter system inserted at one of the two copies of the native locus. Without the addition of doxycycline, these strains over-express *NCP1* at ~8-fold the level of wild-type *NCP1* expression; with the addition of doxycycline, *NCP1* is expressed at 0.5-fold relative to its expression in wild-type cells (S4 Fig B). Overexpression of *NCP1* in these engineered strains resulted in a 2-fold increase in MIC_{50} that was abolished with the addition of doxycycline (S4 Fig C). Because there is allelic variation at the *NCP1* locus in SC5314, we overexpressed the A and

B alleles independently; both *NCP1* alleles resulted in the same 2-fold increase in MIC_{50} (S1 Table). Thus, overexpression of *NCP1* is sufficient to increase growth in low drug concentration and provides at least one explanation for the increased MIC_{50} in the single colonies carrying the Chr4 CNV. However, overexpression of *NCP1* cannot explain the MIC_{50} of >256 µg/mL FLC displayed by passages 4-10 of the evolution experiment.

LOH at *KSR1* produces a high resistance phenotype

To identify the genetic changes responsible for the high level of resistance seen in passages 4-10, we examined the genomes of 5 single colonies from passage 4 and measured their growth across a range of FLC concentrations. All 5 colonies contained the Chr4 CNV (S3 Fig E); however, only 1 of the 5 colonies, isolate P4.5, grew significantly faster than the progenitor in 256 µg/mL FLC and had an MIC_{50} of >256 µg/mL FLC (S1 Table, Fig 1G). Interestingly, P4.5 contained a short (711 bp) LOH of the ChrR B homolog between coordinates 1604191 to 1604902 that was not present in the other colonies. Population-level sequencing of each passage showed that allele ratios in this region were biased for allele A in passages 1-3 but switched to a bias for allele B in passage 4 and steadily rose to 100% frequency of the B allele by passage 9 (Fig 1H). This ~700 bp LOH (which we will now call LOH1) encompassed ~⅔ of *KSR1* (CR_07380C) which encodes 3-ketosphinganine reductase (Fig 1I) and catalyzes the second step in sphingolipid biosynthesis [37].

To directly test the effect of the 711 bp LOH at *KSR1* (*KSR1* LOH1) on drug resistance, we replaced this portion of the *KSR1A* allele with *KSR1B*, reconstructing the evolved LOH in the progenitor background (SC5314) (without the Chr4 CNV). This strain, (*KSR1* LOH1) grew faster than the progenitor at FLC concentrations from 1 to 256 µg/mL, with an MIC_{50} of 8 µg/mL FLC

and an SMG of 0.86 (Fig 1J). Thus, *KSR1* LOH1 alone is sufficient to cause a 16-fold increase in resistance and a high tolerance phenotype (~8-fold higher than the progenitor).

Next, we tested the hypothesis that overexpression of *NCP1* and the *KSR1* LOH1 in combination could explain the evolved resistance phenotype. A strain engineered to carry both the *tetO-NCP1* overexpression construct and the *KSR1* LOH1 genotype (tetO-*NCP1*,*KSR1* LOH1) grew faster than either single mutant alone in low and high FLC. However, the strain with tetO-*NCP1* and *KSR1* LOH1 had a final MIC_{50} of 4 and SMG of 0.66 (S5 Fig), which is not sufficient to reproduce the MIC_{50} of single colony P4.5, which carried the ~150kb Chr4 CNV and the *KSR1* LOH1. This implies that one or more additional genes within the Chr4 CNV might be necessary, in combination with the *KSR1* LOH1, to account for the high MIC_{50} of the populations at passages 4-10 and of single colony P4.5. Additionally, amplification of the Chr4 CNV coincided with LOH of Chr4 sequences that flank the CNV (S2 Fig C). Therefore, we cannot rule out the possibility that LOH of other genes on Chr4 could contribute to high resistance in strain P4.5 as well.

To ask if Ksr1p is necessary for drug resistance, we tried to engineer null strains lacking both copies of *KSR1*. We obtained heterozygous mutants by deleting either the A or B allele individually. Strains lacking the *KSR1* B allele had a wild-type MIC_{50} of 0.5 μg/mL FLC, while strains lacking the *KSR1* A allele had an MIC_{50} of 2 μg/ml FLC, a 4-fold increase relative to the parent strain (S6 Fig A). Despite several attempts in multiple labs, the only two *ksr1Δ/Δ* transformants recovered had undergone large LOHs encompassing most of ChrR (S6 Fig B), which confounded the interpretation of phenotypes associated with the complete loss of Ksr1p. In *Saccharomyces cerevisiae,* the *KSR1* ortholog (*TSC10*) is essential [52]; however, in *C. albicans,* null mutants of *KSR1* (strains SC90, SC91) were previously described in strain BWP17, an auxotrophic derivative of SC5314 [37]. Whole genome sequencing of these original

BWP17 *ksr1Δ/Δ* null strains revealed that both mutants had also undergone LOH encompassing most of ChrR (S6 Fig B). Interestingly, two of the four *ksr1Δ/Δ* null strains were homozygous for ChrR AA (blue) and the other two were homozygous for ChrR BB (pink), but in all four strains the region flanking the *KSR1* locus was homozygous for the A allele (AA) (S6 Fig C). Importantly, other manipulations of *KSR1* usually were not accompanied by large LOHs (see below), suggesting that *KSR1* might be essential in the SC5314 background when ChrR maintains normal heterozygosity.

KSR1 LOH1 results in reduced sphingolipids, lower intracellular FLC, and higher drug efflux

Ksr1p catalyzes an early step in sphingolipid biosynthesis (S1 Fig) and changes in its function may alter the cellular sphingolipid composition [37,53,54]. Consistent with this, *ksr1Δ/Δ* strains (SC90 and SC91, containing large ChrR LOH regions) had lower levels of inositol phosphorylceramides and were sensitized to inhibitors of subsequent steps of sphingolipid biosynthesis [37]. To determine the role of the evolved *KSR1* LOH1 we compared the lipid content of the progenitor (SC5314) and *KSR1* LOH1 (engineered into SC5314), with and without FLC treatment, using mass spectrometry. In the absence of FLC, the abundance of all sphingolipid species was reduced in the *KSR1* LOH1 strain relative to the progenitor (Fig 2A). In the progenitor, upon FLC exposure (1 and 10 μg/mL) intermediates of the sphingolipid pathway increased and glucosylceramides decreased in abundance (Fig 2A). By contrast, the *KSR1* LOH1 strain had consistently low levels of both phytosphingolipids and glucosylceramides. In addition, exposure of the *KSR1* LOH1 strain to 10 μg/mL FLC resulted in increased sphingosine (Sph), phosphorylated dihydrosphingosine (dhSph-1-p) and phosphorylated phytosphingosine (PhytoSph-1-p) relative to no drug conditions, in two of the three replicates (Fig 2A, green box). No such change in sphingolipid species was seen in the progenitor. Together, these results

indicate that in general, sphingolipid species are decreased in the *KSR1* LOH1 strain relative to the progenitor strain, and that the two strains respond differently to FLC.

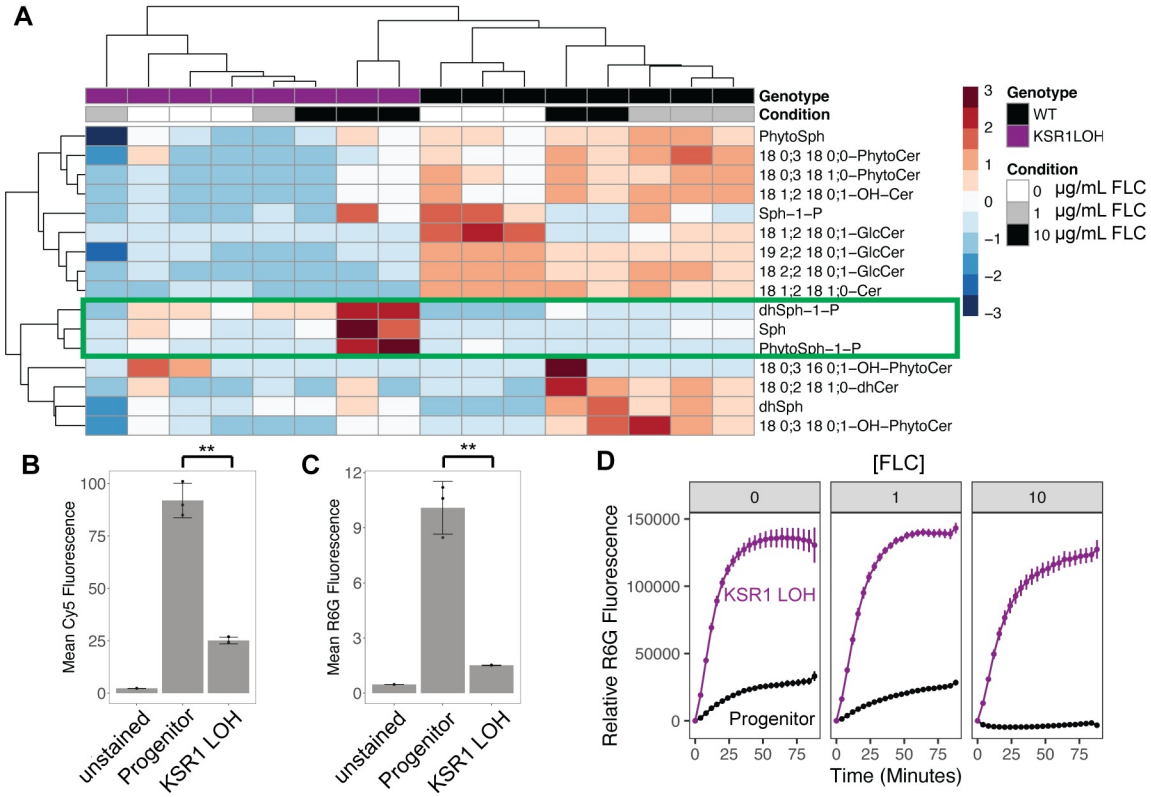

Fig 2. LOH at *KSR1* affects cellular lipid profiles, intracellular FLC concentrations, and drug efflux. (A) A heatmap shows abundance of sphingolipid species relative to inorganic phosphate present in each strain and condition relative to the mean of all samples for each respective lipid species. Heatmap colors indicate row-wise z-scores, red being high and blue being low. Rows are lipid species and columns are individual samples, both of which are clustered by k-means clustering as shown by the dendrograms on the top and left. Columns include 3 replicates each of the wild type progenitor strain (black) grown in 0 µg/mL (white), 1 µg/mL (grey), and 10 µg/mL FLC (black), and the *KSR1* LOH1 engineered strain (purple) in the same conditions. Two outlier samples were removed (WT in 10 µg/mL FLC and *KSR1* LOH1 in 1 µg/mL FLC). Wild type samples cluster according to condition, indicating consistent changes in sphingolipid species as FLC concentrations are increased. *KSR1* LOH1 samples do not

consistently cluster by condition, indicating only subtle changes in sphingolipid species as FLC concentration increases. Sphingolipid species (rows) that increase in the *KSR1* LOH1 strain at high FLC concentration are boxed in green. (B) Mean intracellular Cy5 fluorescence, as measured by flow cytometry, is plotted with both points and bars for each strain listed after 4 hours of incubation with Cy5-FLC. Each point represents one replicate, bars are means and whiskers are quartiles. (**Indicates a paired t-test p-value of < 0.01) (C) As in (B), mean intracellular R6G fluorescence is plotted for each strain listed after incubation with rhodamine 6G for 4 hours. (D) Extracellular R6G fluorescence is plotted on the y-axis over time (on the x-axis) after addition of glucose, for the progenitor strain (black) and engineered *KSR1* LOH1 (purple). Points are means and error bars are standard errors of the mean across 3 replicates.

A reduction in sphingolipid species could significantly alter membrane structure, membrane fluidity, and the formation of lipid rafts, which help properly position membrane-associated proteins such as the drug efflux pump Cdr1p [23]. In addition, PhytoSph-1-P is thought to be a signaling molecule that can lead to the upregulation of drug efflux pumps such as Cdr1p and Cdr2p and a reduction in intracellular FLC [32]. Thus, changes in the sphingolipid composition and structure of the cell membrane might influence the ability of drug efflux pumps to export FLC.

To evaluate the effect of *KSR1* LOH1 on FLC export, we measured intracellular drug concentrations by flow cytometry of cells after incubation for 4 hours with a fluorescently labeled FLC probe (FLC-Cy5, [55]). The *KSR1* LOH1 strain had significantly lower intracellular levels of FLC than the progenitor strain at 4 hours (Fig 2B, paired t-test p-value = 0.004). To measure general efflux activity, we monitored intracellular levels of Rhodamine 6G (R6G), a fluorescent molecule that is actively effluxed by ABC transporters [56], by flow cytometry after incubation for 4 hours. *KSR1* LOH1 intracellular R6G levels were ~3-fold lower than in the progenitor strain

(Fig 2C, paired t-test p-value = 0.009). To measure the dynamics of active drug efflux, we performed a time-course in which cells were preloaded with R6G, and fluorescence of the supernatant was measured over time after the addition of glucose. The *KSR1* LOH1 strain had a ~6-fold increase in the rate of efflux relative to the progenitor strain after growth in 0, 1, and 10 µg/mL FLC (Fig 2D). In addition, using RT-qPCR, we found that, relative to the progenitor, *CDR1* was upregulated ~1.5 fold in the absence of FLC, and ~2 fold in 1 µg/mL FLC (S7 Fig). While this increase in expression likely contributes to the higher rate of efflux, the much more dramatic increase in efflux (~6-fold increase in rate, Fig 2D) suggests that additional mechanisms influence efflux activity. Together, these results indicate that cells with the *KSR1* LOH1 have higher rates of drug efflux and accumulate lower levels of intracellular FLC than the progenitor strain.

Chr4 CNV does not increase ceramides in a wild type *KSR1* background

Ceramides, a class of sphingolipids, are important for drug resistance [24] and also reduce the growth rate of aneuploid cells in *S. cerevisiae* [57]. However, it is not known if segmental aneuploidies result in higher ceramide levels and slower growth in *C. albicans*, as they do in *S. cerevisiae*. Therefore, we asked if ceramide levels were elevated in a strain bearing the Chr4 CNV by comparing mass spectrometry data for strain P4.4 (which carries the Chr4 CNV but no LOH at *KSR1*) to the progenitor. Ceramides were not significantly up-regulated in strain P4.4 (two-sample t-test p-values for 0 µg/mL FLC: glycosyl ceramides = 0.53, hydroxy-ceramides = 0.67, ceramides = 0.54, hydroxy-phytoceramides = 0.19, S8 Fig). Ceramide levels were reduced in strain P4.5, which carried both the Chr4 CNV and *KSR1* LOH1, much like the *KSR1* LOH1 alone (S8 Fig). These data suggest that CNVs in *C. albicans* might not incur the same changes in ceramides as those described for aneuploidy in *S. cerevisiae* and is consistent with

the lack of a fitness cost for the Chr4 CNV strains relative to the progenitor (Fig 2B, P4.4 in 0 µg/mL FLC). Therefore, *KSR1* LOH1 likely does not alleviate a fitness cost of the Chr4 CNV. Rather, the Chr4 CNV and *KSR1* LOH1 appear to operate additively to produce increased FLC resistance, as might be expected for two mutations that are acting on two distinct mechanisms of drug resistance that co-evolved in the same cells during adaptation to drug.

Homozygosis of arginine at Ksr1p aa189 is the major driver of drug resistance

To examine the effects of specific amino acid(s) in Ksr1p that contribute to the drug resistance phenotype, we compared *KSR1* LOH1 to three other independently evolved SC5314-strains that acquired *KSR1* LOH events during adaptation to 1 µg/mL FLC (Evolved LOH2, Evolved LOH3, Evolved LOH4, see Methods). These three evolved LOH events ranged in size from ~20 bp to ~2,000 bp of ChrR and each included a portion of the *KSR1* locus (Fig 3A, S9 Fig A, S1 Table). All three evolved strains had 4-fold increases in MIC_{50} and increased SMG relative to the progenitor strain (Fig 3B). They also were defective in filamentation and had decreased virulence in a *Galleria mellonella* model of systemic fungal infection (S9 Fig B-D).

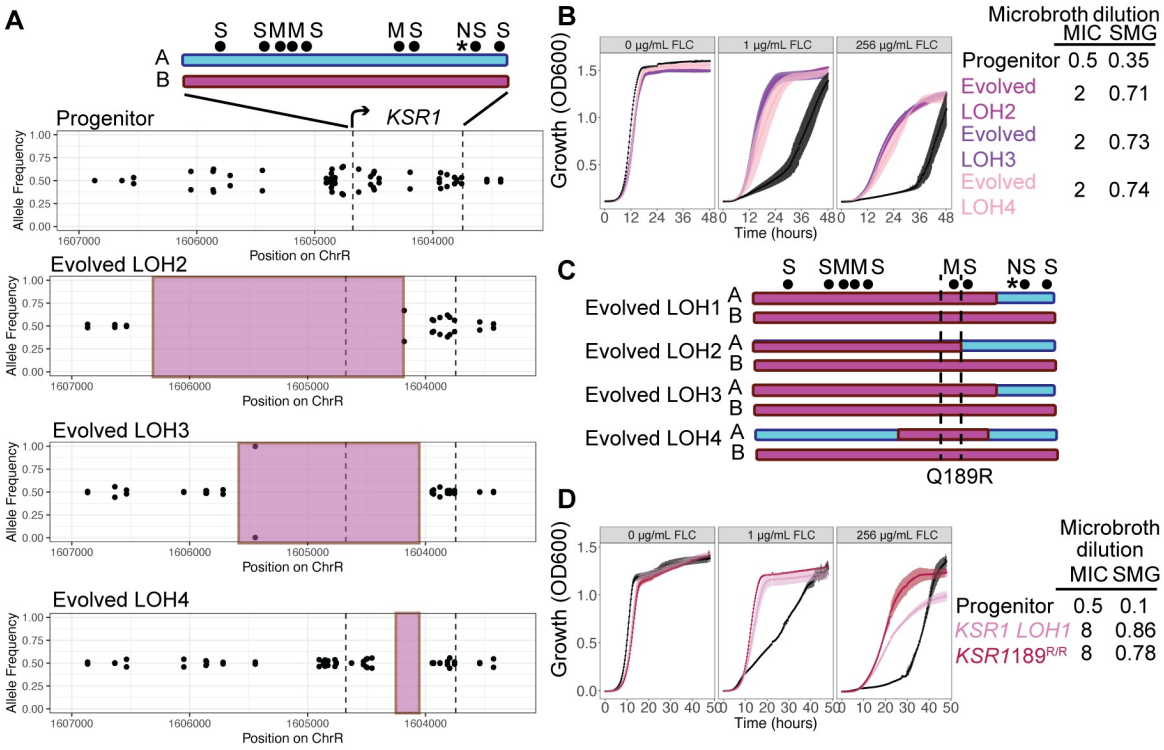

406

407 **Fig 3. LOH resulting in 189R/R produces a strong drug resistance phenotype.** (A) A
408 schematic of the *KSR1* locus including heterozygous positions (black dots) that are either
409 synonymous (S), missense (M), or nonsense (N, *) in the B allele relative to the A allele. A allele
410 is shown in blue and B allele is shown in pink. Allele frequencies are plotted across the *KSR1*
411 locus and a larger flanking region on chromosome R for the wild type progenitor (top) and the
412 three evolved isolates (Evolved LOH2, Evolved LOH3, and Evolved LOH4). The absence of
413 biallelic SNVs in the evolved isolates, or allele frequencies of 1, indicates a loss of
414 heterozygosity in that region highlighted by the pink shaded region. Note that the chromosome
415 coordinates are inverted on the map because the *KSR1* coding sequence is on the '*Crick*'
416 strand of the chromosome. (B) OD_{600} values for liquid culture growth assays are plotted over
417 time for the wild type progenitor (SC5314, black), and the three evolved strains with LOH
418 including some portion of the *KSR1* locus (Evolved LOH2, Evolved LOH3, and Evolved LOH4).
419 Growth in rich media with 0 µg/mL, 1 µg/mL, and 256 µg/mL FLC are shown. Error bars are
420 standard errors for three replicates. MIC_{50} and SMG values are shown in a table to the right. (C)

Schematics show portions of the *KSR1* coding region that underwent LOH in the four evolved LOH events. Dotted lines demarcate the single nonsynonymous SNV that was homozygous in all four LOH isolates, a nucleotide coding for glutamine in allele A and arginine in allele B at amino acid position 189. (D) Liquid growth assays, plotted as in (B), are shown for the progenitor strain (black), the strain engineered to contain the *KSR1* LOH1 (pink), and the *KSR1*$^{189R/R}$ engineered strain (red). MIC_{50} and SMG values are shown in a table to the right.

RNA-sequencing of these three evolved strains when exposed to 0, 2, or 64 μg/mL FLC concentrations was analyzed for principal components. The first principal component, explaining the majority of the variance in the data (83%), separated samples by FLC treatment (S10 Fig A). The second principal component, explaining 5% of the variance in the data, separated strains that were exposed to FLC by genotype (S10 Fig B). This indicates that both wild type and evolved strains undergo major transcriptional changes upon exposure to FLC, and that, in the absence of FLC, transcriptional differences between progenitor and evolved strains are minimal. Expression levels of genes annotated as related to sphingolipid biosynthesis showed a similar trend, with samples clustering according to FLC exposure first, and then clustering weakly by genotype (S10 Fig C). Although 5 genes catalyzing steps in sphingolipid biosynthesis were differentially expressed in all three evolved strains relative to the progenitor strain, no strong correlation between transcriptional changes and changes in corresponding sphingolipid metabolites was evident (S10 Fig D), likely because most upregulated genes were downstream of *KSR1* in the biosynthesis pathway (S1 Fig). Because the *KSR1* LOH1 strain had high levels of glucose-dependent efflux in the R6G assay (Fig 2D), we also examined the expression of ABC drug efflux pumps. Efflux pumps *CDR1* and *CDR2* were not significantly upregulated in the three evolved strains (S10 Fig E). *SNQ2*, which is annotated as a multidrug transporter in *S. cerevisiae* [58], was upregulated in all three strains (S10 Fig E). Taken together, these data indicate that LOH affecting Ksr1p has a small effect on the global transcriptome and likely

447 impacts the activity and/or localization of drug efflux pumps post-transcriptionally, and that the
448 progenitor and evolved strains respond differently to FLC exposure.
449
450 In SC5314, the *KSR1* protein coding region harbors 6 synonymous and 4 nonsynonymous
451 heterozygous nucleotides. The LOH events in all four FLC-evolved LOH strains became
452 homozygous for the B allele at a single nonsynonymous variant encoding aa189 (Fig 3C). In the
453 wild-type SC5314, allele A encodes glutamine and allele B encodes arginine ($KSR1^{189Q/R}$); in all
454 four evolved LOH isolates (LOH1-LOH4) the sequence encodes arginine at aa189 ($KSR1^{189R/R}$).
455 To test the effect of aa189R/R alone, we constructed a strain encoding $KSR1^{189R/R}$ and
456 measured its growth in a range of FLC concentrations. The $KSR1^{189R/R}$ strain was more resistant
457 (MIC_{50} of 8 μg/mL) and tolerant (SMG of 0.78) and grew better than the progenitor across FLC
458 concentrations (Fig 3D), with growth dynamics similar to those of the *KSR1* LOH1 strain in 1
459 μg/mL FLC and better than the growth of *KSR1* LOH1 in 256 μg/mL FLC. Thus, $KSR1^{189R/R}$ is a
460 major driver of resistance in all four evolved strains (Fig 3D).
461

462 LOH unlinks the effect of 189R/R from the masking effect of
463 the nonsense codon

464 *KSR1* codon 272 in the SC5314 progenitor encodes arginine on the A allele and encodes a
465 nonsense mutation on the B allele ($KSR1^{272R/*}$). Notably, all four LOH events in FLC-resistant
466 strains remained heterozygous at this codon ($KSR1^{272R/*}$, Fig 3C). We asked if a strain carrying
467 the homozygous nonsense allele would be viable, and if so, if the nonsense allele would mask
468 the effect of aa189R/R on drug resistance. To address these questions, we engineered mutants
469 that were homozygous for the nonsense codon ($KSR1^{272*/*}$) and mutants that were homozygous
470 for the entire B allele (*KSR1B/B*, which is homozygous for both aa189R/R and aa272*/*) (Fig
471 4A). We were able to recover both mutants without any additional LOH events (S11 Fig), and

found that both *KSR1*$^{272*/*}$ and *KSR1B/B* had increased MIC_{50} and SMG values (MIC_{50} = 4 µg/mL, SMG = 0.86) relative to the progenitor SC5314 (MIC_{50} = 0.5 µg/mL, SMG = 0.01, Fig 3D), but the MIC_{50} was not elevated to the same degree as *KSR1* LOH1 (MIC_{50} = 8 µg/mL, SMG = 0.86, Fig 4A,B). Furthermore, growth curve analysis across a range of FLC concentrations determined that the average growth of *KSR1B/B* and *KSR1*$^{272*/*}$ was nearly identical and consistently lower than *KSR1* LOH1 at drug concentrations > 1 µg/mL (Fig 4B, paired t-test between *KSR1* LOH1 and *KSR1B/B* p-values < 0.1). The matched growth of *KSR1*$^{272*/*}$ and *KSR1B/B* (which includes aa189R/R and aa272*/*), indicates that homozygosis of the nonsense codon affects drug resistance itself and masks the effect of 189R/R in strains carrying both 189R/R and 272*/*.

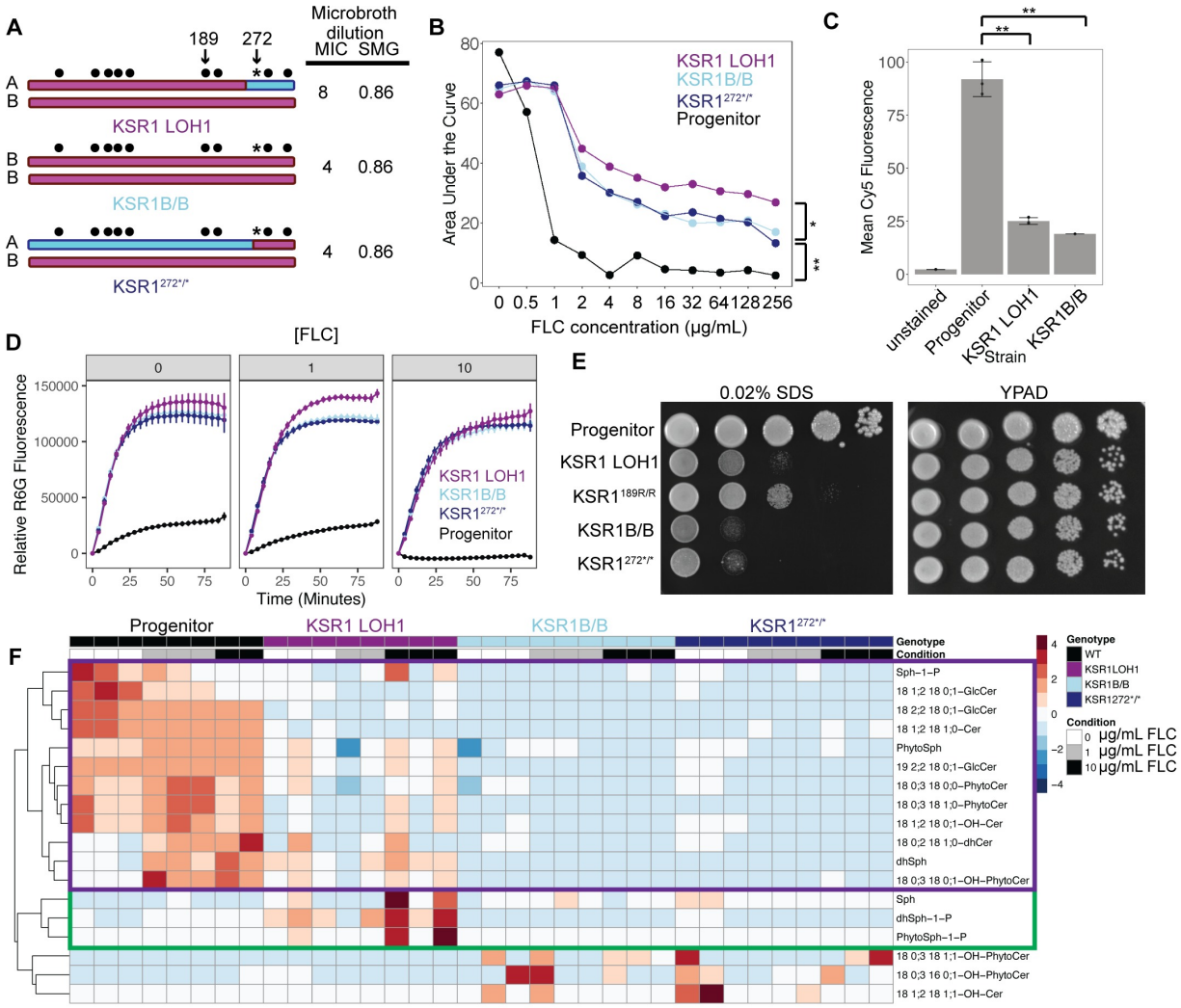

Fig 4. LOH unlinks 189R/R from a stop codon with masking effects on phenotype.

(A) Schematics of the *KSR1* locus in three engineered strains: the strain engineered to contain the *KSR1* LOH1 (as in Fig 2C), one that is completely homozygous for the *KSR1B* allele (*KSR1B/B*), and one that is homozygous for the nonsense codon to the end of the protein (*KSR1*$^{272*/*}$). SNP positions are indicated by circles, and the SNP that codes for the nonsense codon in allele B is indicated by an asterisk. A and B alleles are indicated in blue and pink, respectively. (B) Area under the growth curve, calculated from 48 h liquid growth assays, is plotted on the y-axis, relative to the growth condition of various FLC concentrations shown on the x-axis. Each point is the mean of three replicates. Each strain is shown in a different color

and connected by line segments. (*Indicates paired t-test values < 0.1, ** indicates paired t-test values < 0.01 for all comparison in 2ug/mL FLC and higher) (C) Mean intracellular Cy5 fluorescence, as measured by flow cytometry, is plotted with both points and bars for each strain listed, after 4 hours of incubation with FLC-Cy5. Each point represents one replicate, bars are means and whiskers are quartiles. The same data as shown in Fig 2B is shown with the addition of the *KSR1B/B* strain for comparison. (**Indicates a paired t-test p-value of < 0.01) (D) Extracellular R6G fluorescence is plotted on the y-axis over time after the addition of glucose, measured in minutes, on the x-axis. The same data as shown in Fig 2D is shown with the addition of a *KSR1B/B* (light blue) and *KSR1*$^{272*/*}$ (dark blue) strain for comparison. (E) Spot plates showing serial dilutions of strain across the x-axis at concentrations of 10^7, 10^6, 10^5, 10^4, and 10^3 cells/mL in rich media (YPAD), and 0.02% sodium dodecyl sulfate (SDS). One representative replicate of 3 performed is shown. (F) A heatmap showing levels of sphingolipid species present in each strain and condition relative to the mean among all samples for that lipid species. Heatmap colors indicate row-wise z-scores, red being high and blue being low. Rows are lipid species, clustered by k-means clustering as shown by the dendrograms on the left, and columns are individual samples, which are not clustered. Columns include 3 replicates each of the wild-type progenitor strain (black) grown in 0 μg/mL (white), 1 μg/mL (grey), and 10 μg/mL FLC (black), and the *KSR1* LOH1 engineered strain (purple), the *KSR1*B/B strain (light blue) and *KSR1*$^{272*/*}$ (dark blue) in the same conditions.

We next asked if homozygosis of the nonsense codon 272*/* and homozygosis of 189R/R affect drug resistance via similar mechanisms by measuring intracellular levels of FLC at 4 and 24 hours after drug exposure. We found that both *KSR1* LOH1 and *KSR1B/B* strains accumulated less intracellular FLC relative to the progenitor strain (Fig 4C, paired t-test p-value for *KSR1B/B* = 0.004). Furthermore, *KSR1* LOH1, *KSR1*$^{272*/*}$, and *KSR1B/B* all had increased active efflux of R6G when exposed to 0, 1, or 10 μg/mL FLC (Fig 4D). All three mutants also had a heightened

sensitivity to the detergent SDS, which destabilizes cell membranes (Fig 4E). Interestingly, the strains with a homozygous nonsense codon (*KSR1B/B* and *KSR1*$^{272*/*}$) had a stronger growth defect in the presence of SDS relative to the *KSR1* LOH1 strain (Fig 4E). Thus, all mutants had similar intracellular FLC levels and efflux levels, but those with a homozygous nonsense codon were more sensitive to SDS, suggestive of a more severe membrane defect.

We next asked about differences in the sphingolipid composition of *KSR1* LOH1 relative to strains homozygous for the nonsense codon. By comparing lipidomic data for the *KSR1* LOH1, *KSR1B/B,* and *KSR1*$^{272*/*}$ strains and the progenitor, we found that strains homozygous for the nonsense mutation had lower levels of all sphingolipid species relative to both the progenitor and the *KSR1* LOH1 strain (Fig 4F, purple box). In addition, strains homozygous for the nonsense mutation did not have the increase in dhSph-1-p or PhytoSph-1-p that was seen in the *KSR1* LOH1 strain relative to the progenitor at 10 µg/mL FLC (Fig 4F, green box). Together, these results suggest that both *KSR1* LOH1 and strains homozygous for the nonsense codon have increased drug resistance due to increased drug efflux related to changes in their sphingolipid composition, and that changes in sphingolipid levels are more severe in strains homozygous for the nonsense codon.

The SDS sensitivity of the strains prompted us to examine their vacuole morphology, which can be an indication of membrane stress [35]. Indeed, using FM4-64 to stain vacuolar membranes, we observed some vacuolar abnormality: in FLC, both *KSR1* LOH1 and *KSR1B/B* strains had smaller vacuolar area than the progenitor strain (S12 Fig A,B), yet were similar in size and morphology to the progenitor strain (S12 Fig A).

Lipid droplets affect cellular stress responses by sequestering excess toxic lipids and sterols and mediating the release and transport of lipids from the ER to the plasma membrane and

other cellular organelles [59]. Using BODIPY staining to visualize lipid droplets, we found that the *KSR1* LOH1 strain had, on average, a higher, but not significantly different, number of lipid droplets per cell as compared to the progenitor, in rich media. Conversely, the *KSR1B/B* strain had, on average, a significantly lower number of BODIPY stained lipid droplets, which was similar to the decrease in the number of lipid droplets seen when wild-type cells were treated with myriocin (S13 Fig A,B). Since myriocin inhibits the step in sphingolipid biosynthesis immediately preceding the reaction catalyzed by *KSR1* [33,34], this indicates that *KSR1B/B* shares a phenotype characteristic of sphingolipid pathway inhibition while the *KSR1* LOH1 does not. Together, these results indicate that *KSR1* LOH1 as well as strains with homozygous nonsense codon affect lipid homeostasis, membrane stress, and the formation of lipid droplets, but that these two types of mutations differ in their effect on lipid droplet properties.

Nonsense codon at aa272 results in mislocalization of Ksr1p

The *KSR1* nonsense codon is predicted to truncate the protein immediately upstream of a putative membrane-anchoring domain encoded by *KSR1A* in *C. albicans* and in *TSC10,* the *S. cerevisiae* ortholog (Fig 5A, [37,60,61]). To ask if this C-terminal tail affects Ksr1p localization, we fused an mNeon-Green fluorescent protein to the N-terminus of either *KSR1A* or *KSR1B* in the SC5314 background. As expected based on the localization of Tsc10p in *S. cerevisiae,* mNeonGreen-Ksr1A co-localized with an ER stain. However, mNeonGreen-KSR1B labeling was diffuse throughout the cytoplasm (Fig 5B). We posit that the failure of the truncated Ksr1Bp to localize to the ER likely prevents efficient contact of Ksr1p with its substrate, which is in the ER, and thus effectively reduces Ksr1Bp activity. The reduction in activity due to mislocalization appears more severe than that resulting from the homozygosis of arginine at aa189, based on the further reduction in sphingolipid species abundance in strains with homozygous nonsense alleles (Fig 4F). However, rather than further increasing drug efflux and drug resistance, efflux in

569 these strains remained steady (Fig 4C,D), and sensitivity to SDS was increased (Fig 4E).
570 Together, these data suggest that cumulative positive and negative fitness trade-offs result in a
571 'sweet spot' for drug resistance that is occupied by the evolved strains with *KSR1*$^{189R/R}$ but not in
572 those harboring homozygous nonsense codons (Fig 5C). This underscores the observation that,
573 at the end of the evolution experiments, all four LOH events homozygosed *KSR1* aa189 but not
574 aa272.
575

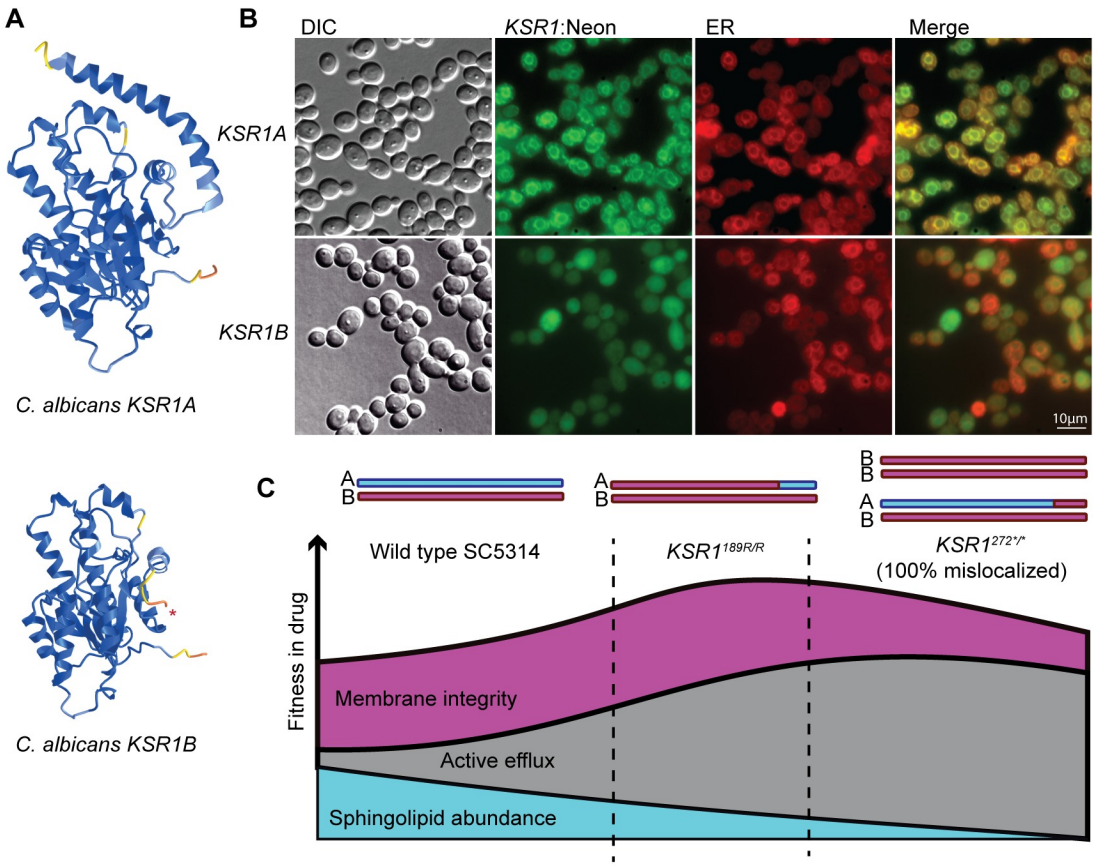

Fig 5. Nonsense allele results in mislocalization of Ksr1p (A) Ribbon models produced by Alphafold [60] predictions are shown for *C. albicans* Ksr1pA and Ksr1pB. The early stop codon in Ksr1pB (red star) truncates the protein ahead of a putative membrane-anchoring domain positioned on the right side of the model. Models are colored according to Alphafold confidence scores, in which blue is high and yellow to red are low. (B) Fluorescence microscopy images for engineered strains containing *KSR1A* (top row) or *KSR1B* (bottom row) tagged with NeonGreen. From left to right the columns show DIC, Neon green fluorescence, the endoplasmic reticulum-specific probe 2 [66], and a merged image of mNeonGreen and ER probe. (C) A model reflecting the levels of sphingolipid abundance, rate of active efflux, and membrane sensitivity together contributing to a theoretical fitness landscape. The regions on this landscape occupied by a completely wild-type Ksr1p (left), a localized *KSR1*$^{189R/R}$ mutant such as the LOH strains (middle), and strains with a homozygous nonsense mutation resulting

589 in mislocalization (right) are shown. The evolved LOHs occupy a 'sweet spot' for drug
590 resistance, with increased active efflux, intermediate sphingolipid levels, and membrane
591 sensitivity leading to the highest drug resistance and tolerance.
592

593 # Discussion

594 Here we followed the evolutionary progression of a lineage of *C. albicans* adapting to the azole
595 drug fluconazole via the sequential acquisition of CNV followed by LOH on a different
596 chromosome occurring in the same background. Each of these genome changes affected many
597 genes, yet we found that much of the resistance can be attributed to changes in two genes:
598 amplification of *NCP1* within the Chr4 CNV and partial homozygosis of *KSR1* within the ChrR
599 LOH. These two genes were not previously associated with drug resistance and it appears that
600 they impact resistance via different mechanisms. *NCP1* encodes a cytochrome p450 reductase
601 that, when overexpressed, increases the FLC MIC_{50} by 2-fold. Ncp1p was a likely contributor to
602 drug resistance because it interacts with Erg11p, the target of fluconazole. In addition, a screen
603 for haploinsufficient increases in drug sensitivity did identify an *NCP1* heterozygous null as a
604 sensitizer to FLC [62]. However, we are not aware of any previous descriptions of *NCP1* copy
605 number changes conferring increased FLC resistance. The Chr4 CNV was followed by a ChrR
606 LOH event that homozygosed part of *KSR1,* which is required for proper sphingolipid
607 biosynthesis. The homozygosis of codon 189 to arginine can explain a 16-fold increase in the
608 MIC_{50} as well as a high level of drug tolerance. When in combination with the Chr4 CNV, these
609 two mutations are associated with an MIC_{50} of >256 μg/mL FLC. Interestingly, the combination
610 of an overexpression of *NCP1* and LOH at *KSR1* does not phenocopy the combination of the
611 Chr4 CNV and LOH at *KSR1*, indicating other genes located in the Chr4 CNV that might also
612 contribute to drug resistance or interact with the LOH at *KSR1*.
613

LOH of *KSR1* arose independently in four isolates that were selected for increased growth in fluconazole. Recurrent isolation of similar LOH breakpoints points to the potential importance of Ksr1p and sphingolipid metabolism in drug responses. All four independently evolved *KSR1* mutants were defective in filamentation, a phenotype also seen previously with *ksr1*Δ/Δ mutants [37]. We posit that the filamentation defect in *KSR1* mutations might be due to alterations in the levels of sphingolipids and ergosterol that perturb lipid raft formation and cell membrane polarization, processes critical to filamentous growth [22,63]. The filamentation defect might also lead to a decrease in virulence, which could help explain why *KSR1* mutants have not been previously identified in azole resistant clinical isolates. However, the biosynthesis of sphingolipids, and specifically glucosyl ceramides, is also required for *C. albicans* virulence independently of the yeast-to-hyphal transition [64]. The precise connection between sphingolipids, filamentation, and virulence remains to be determined [24].

One remarkable feature of the four independent LOH events observed at *KSR1* is that they all effectively unlinked two loci: codon 189, a residue important for resistance, was homozygosed, while codon 272, which encodes a premature stop codon, always remained heterozygous. The power of LOH to act as a type of allelic recombination might help explain the lack of a predicted 'genetic breakdown,' also known as Muller's ratchet [65], observed in asexual diploid species, in which stop codons or loss of function mutations are allowed to accumulate with deleterious effects [40].

The nonsense allele at codon 272 truncates Ksr1p just prior to its localization domain and consequently results in Ksr1p mislocalization. The mislocalization of Ksr1p likely inhibits its ability to interact with its substrate in the ER, greatly diminishing enzyme efficiency. However, the nonsense mutation in *KSR1B* does not appear to be a null allele, based on our ability to obtain *KSR1B/B* transformants. We propose that, as in other fungal species [54], Ksr1p forms a

640 homodimer. In a strain heterozygous for the nonsense codon at *KSR1*, localization of Ksr1p
641 would be only partially reduced, because heterodimers would be able to localize partially, while
642 homodimers would fail to localize properly. Thus, we propose that complete Ksr1p
643 mislocalization severely reduces sphingolipid levels, affecting the cell membrane structure and
644 resulting in an increase in active drug efflux (Fig 5C). By contrast, 189R/R homozygosity
645 localizes to the ER and only partially inhibits sphingolipid biosynthesis. Thus, 189R/R
646 homozygosis results in a 'sweet spot' for drug resistance, in which efflux is highly active and the
647 membrane is not as severely compromised (Fig 5C).
648
649 *KSR1* Arg189 is predicted to lie at the interface between the two subunits of the dimer in
650 *Cryptococcus neoformans*, where the structure of the homodimer was recently solved [54], and
651 it also is in close proximity to the well-conserved catalytic triad [37]. Therefore, homozygosity of
652 arginine at amino acid 189 could influence dimerization, enzymatic specificity and/or enzyme
653 activity. Based on the observed reduction in sphingolipid species, 189R/R appears to reduce
654 Ksr1p function relative to the progenitor that is heterozygous (189R/Q). Interestingly, inhibition
655 of sphingolipid biosynthesis with myriocin, NPD827 or aureobasidin A, increases FLC sensitivity
656 rather than increasing FLC resistance [33–35]; similarly, other loss of function mutations in
657 sphingolipid genes tend to decrease, rather than increase FLC resistance [24,32]. This does not
658 appear to be the case for *KSR1* and suggests that the relationship between drug resistance and
659 sphingolipid abundance phenotypes may be more complex than previously appreciated. Indeed,
660 although connections have been made between sphingolipid abundance and the activity of drug
661 efflux pumps, exactly how these two are connected remains to be determined.
662
663 In summary, here we observed an increase in tolerance early in the evolution experiment that
664 was associated with the early appearance of CNV and aneuploidy, followed by the acquisition of
665 a short LOH event that resulted in strong azole resistance. Both CNV and LOH occur at higher

frequencies than de-novo point mutations [5–8], and therefore the co-occurrence of these types of mutations in the same background is likely. The LOHs we observe here are short, much like gene conversion events, and could therefore easily be overlooked in genome sequencing. Indeed, despite their importance, identifying CNV and LOH remains challenging, particularly in whole-population sequencing. In addition, because they often impact multiple genes, determining the specific genes and mechanisms by which CNV and LOH impact FLC sensitivity is difficult. This study demonstrates that the rapid acquisition of large genome changes and LOH events are frequent enough to co-occur and to rapidly acquire high levels of antifungal drug resistance. This work sheds light on genes that contribute to this process, and further studies elucidating the mechanisms of drug resistance behind other CNV and LOH events will continue to improve our understanding of the forces at play during adaptation to antifungal drugs.

Materials and Methods

Data availability

RNA sequences reported in this paper have been deposited in the NCBI Sequence Read Archive, https://www.ncbi.nlm.nih.gov/bioproject (BioProject ID PRJNA1063495), and whole genome sequencing data for strains described in this paper (S1 Table) have been deposited in NCBI Sequence Read Archive (BioProject ID PRJNA1071177).

Microbroth dilution assays (MIC_{50} and SMG) and growth curve assays

Strains were grown from frozen glycerol stocks overnight in 3 mL of YPAD containing 2% dextrose (20 g/L Bactopeptone, 10 g/L yeast extract, 0.04 g/L adenine, 0.08 g/L uridine). Strains were then diluted to a final calculated OD of 0.01 in YPAD containing 1% dextrose and added to

689 a 96-well assay plate at a 1:10 ratio, resulting in a final starting OD of 0.001 in each well. Assay
690 plates were prepared by performing serial dilutions of YPAD containing 1% dextrose and 256
691 µg/mL fluconazole, resulting in final concentrations of 256, 128, 64, 32, 16, 8, 4, 2, 1, or 0.5
692 µg/mL FLC with cells added, as well as YPAD with 1% dextrose without the addition of FLC.
693
694 For MIC_{50} and SMG assays, 96-well plates were allowed to incubate stationary in a humidified
695 chamber at 30°C for 24 hours, at which time they were resuspended by pipetting and OD_{600}
696 measured using a BioTek Epoch 2 microplate reader. Plates were then allowed to sit stationary
697 for another 24 hours (48 total) at 30°C in a humidified chamber, after which they were
698 resuspended and OD measured. MIC_{50} was calculated by first subtracting blank values from all
699 wells and then normalizing each strain grown in FLC to the same strain grown in YPAD without
700 FLC and then averaged across replicates. The drug concentration at which average growth was
701 reduced below 50% at 24 hours was designated as the MIC_{50}. SMG was calculated by
702 averaging the normalized growth at 48 hours for all concentrations of FLC greater than the
703 MIC_{50} value. The triplicate measurements were averaged to produce the final reported SMG
704 value.
705
706 For growth curves, 96-well plates containing sterilized water motes surrounding the outer wells
707 were prepared as described above for microbroth dilution assays and grown in a BioTek Epoch
708 2 at 30°C with shaking for 48 hours, with OD_{600} readings taken every 15 minutes. Data was
709 analyzed in R (version 4.1.3) using the package growthcurver [68] to calculate empirical AUC
710 values. Mean and SE of triplicate OD_{600} values (minus blanks) were calculated and plotted over
711 time using ggplot2 for all growth curve plots.
712

Evolution experiments

The lineage described in Fig 1 was evolved as previously described in [47]. As detailed there, a single colony isolated from susceptible lab strain SC5314 was suspended in 1 mL sterile YPAD media and grown overnight at 30°C. One fourth of this culture was used to initiate a lineage grown in YPAD + 1 μg/mL FLC in a deep-well 96-well plate which was sealed with Breathe EASIER tape and placed in a humidified chamber at 30°C for 72 hours. Every 72 hours, cells were resuspended and transferred to a new plate with fresh YPAD + 1 μg/mL FLC at a dilution of 1:1000 for a total of 10 transfers. Culture remaining from each passage was frozen at -80°C in 20% glycerol.

In this second experiment, *C. albicans* cells were evolved in liquid YPD (2% bacto-peptone, 1% yeast extract, 2% dextrose (filter-sterilized)) + 1 μg/mL FLC. The experiment consisted of 4 lineages each initiated from a single colony SC5314 progenitor and passaged at a 1:100 dilution every 24 hours for a total of 12 passages (30°C, 200 rpm), approximating 80 generations. Every 4 days, the passaged cultures were frozen at -80°C in 25% glycerol. The final passage of each lineage was frozen at -80°C in 25% glycerol and selected for further analysis.

Whole genome sequencing, variant detection, and allele frequency analysis

To ensure that the results of whole genome sequencing for evolution passages reflected the entire populations as much as possible, each glycerol stocked passage was thawed and half the entire volume used for a short (~16 hours) growth expansion in 0.5 μg/mL FLC before collection of genomic DNA for sequencing. For all other whole genome sequencing experiments, strains were grown in 3 mL YPAD containing 2% dextrose overnight at 30°C with shaking. Cells were

pelleted and resuspended in TENTS buffer (1% SDS, 100 mM NaCl, 100 mM Tris pH 8, 1 mM EDTA, 2% Triton), added to ~250 uL of .5 mm glass beads, and lysed in a BeadRuptor Elite (Omni International, 1 cycle, 4 m/s, 15 s). Genomic DNA was then isolated using a phenol-chloroform extraction. Sequencing libraries were prepared by SeqCenter, LLC, or SeqCoast Genomics using the Illumina DNA Prep and sequenced on an Illumina NovaSeq 6000. Adaptor sequences and low-quality reads were removed using Trimmomatic (v0.39, parameters LEADING:3 TRAILING:3 SLIDINGWINDOW:4:15 MINLEN:36 TOPHRED33) [69]. Trimmed reads were mapped to the *C. albicans* reference genome (A21-s02-m09-r08) from the Candida Genome Database (CGD) (http://www.candidagenome.org/download/sequence/C_albicans_SC5314/Assembly21/). Reads were mapped using BWA-MEM (v0.7.17) with default parameters [70]. Samtools (v1.10) [71] was used to sort, index, and remove PCR duplicates from aligned reads, as well as calculate read depth at each genomic nucleotide position using the 'samtools depth' function. Single nucleotide variants were called using GATK (v4.1.2) [72] Mutect2, with SC5314 designated as the 'normal' sample to identify new SNVs, or with the mutant designated as the 'normal' sample to identify regions of LOH, using default parameters. Variants differing between evolved and progenitor strains were then manually inspected using the Integrated Genome Viewer (IGV, v2.12.3) [73]. Biallelic SNPs for allele frequencies were identified using GATK (v4.1.2) 'HaplotypeCaller' [74] followed by 'GenotypeGVCFs', both set with -ploidy 2, and then selected using 'SelectVariants' with parameters -select-type SNP and –restrict-alleles-to BIALLELIC. Variants were then filtered for quality using QD < 2.0, QUAL < 30.0, SOR > 3.0, FS > 60.0, MQ < 40.0, MQRankSum < -12.5, and ReadPosRankSum < -8.0.

CNV analysis

Whole genome sequencing was processed as described above, and sequencing depth files generated using 'samtools depth' were downloaded and further processed in R (v4.1.3) to identify regions of varying copy number. Depth files were read into R, and rolling means were calculated for 500 bp windows across the entire genome using the RcppRoll R package (v0.3.0) [75]. Means were then divided by the median read depth of the entire genome (excluding mitochondrial DNA) to calculate relative abundance and then multiplied by 2 (due to *C. albicans* being a diploid organism) to generate an estimated copy number. Estimated copy numbers were then plotted according to genomic position to visualize regions of the genome with changes in copy number. Copy number based on read depth and heterozygosity of the entire genome was also visualized using the online YMAP platform [76]. Raw fastq files were uploaded to YMAP and processed using the parameters "ploidy of experiment: 2, baseline ploidy:2, generate Figs with annotations? Yes, data type: whole genome NGS (short reads), read type: paired-end short reads, reference genome: Candida albicans SC5314 (CGD: A21-s02-m09-r10), haplotype map: Abbey_et_al_2014, chromosome-end bias (forces using GC content bias) checked."

For mixed populations, such as the entire passage populations of the first evolution experiment, abundance of trisomies or CNVs in the population was estimated using the copy numbers calculated for individual clones isolated from the populations as a reference. The formula A*x + B*(1-x)= C, where A is euploid copy number, B is the CNV copy number estimated from a single colony, and C is the estimated copy number from the entire population, was used to find x, the proportion of the population containing the CNV, assuming no other CNV of a different copy number is present in the same region.

Strain engineering

All primers and sequences used in strain construction and verification are listed in S2 Table. All strains described in this paper (S1 Table) were whole genome sequenced, and the whole genomes sequencing data can be found at the NCBI Sequence Read Archive (BioProject ID PRJNA1071177).

Construction of *KSR1* LOH1, *KSR1*$^{272*/*}$, *KSR1B/B*, and *KSR1A/A* strains

KSR1 LOH engineered strains, including *KSR1* LOH1, *KSR1*$^{272*/*}$ and *KSR1B/B* were constructed using homologous recombination. Transformation constructs were generated by amplifying three fragments that were subsequently stitched together into one fragment using strand overlap extension PCR: 1) a 398 bp fragment downstream of the *KSR1* locus (relative to the Crick strand) amplified from genomic DNA of the evolved strain containing the KSR1 LOH, 2) a NAT resistance marker optimized for *C. albicans* from plasmid pAS3019, and 3) the entire *KSR1* coding sequence and 464bp immediately upstream (relative to the Crick strand) amplified from genomic DNA of the evolved strain containing the *KSR1* locus. Amplification of the *KSR1* locus to generate the transformation construct was not allele-specific, and therefore a mixed pool of transformation constructs was generated that included both *KSR1B* and the chimeric combination of *KSR1A* and *KSR1B* that resulted from LOH1. Transformation was performed in SC5314 by lithium acetate and heat shock, and single colonies isolated. Single colonies were screened by PCR for correct upstream and downstream insertion into the genome. Sanger sequencing was then performed for the entire *KSR1* locus specifically for the transformed allele by amplifying fragments from within the NAT resistance marker to determine the combination of A and B SNVs present. The genotype of the non-transformed allele was determined by amplification the *KSR1* locus, selection of the smaller band (excluding NAT), and restriction

digest with restriction enzyme BanII, which will cut the A allele sequence at nucleotide 192 (GAGCCC) but not the B allele sequence (GAACCC). In this way, three strains were selected: 1) one in which the entire A allele had been transformed with the new chimeric allele, resulting in the identical genotype to the evolved strain at the *KSR1* locus, 2) one in which the A allele had been partially transformed with the B allele construct, resulting in $KSR^{272*/*}$ that was otherwise heterozygous, and 3) one in which the entire A allele had been transformed into a complete B allele at the *KSR1* locus resulting in *KSR1B/B*. Whole genome sequencing was then performed to ensure the correct genotypes at *KSR1* and ensure that these strains did not contain additional changes such as aneuploidies or other LOH. The same process was used to generate the *KSR1A/A* strain, using genomic DNA from the wild-type SC5314 to amplify the *KSR1A* locus.

Construction of *tetO-NCP1* strains

Strains containing an tetO-*NCP1* overexpression construct were generated by first amplifying a transformation construct using primers with homology to the native *NCP1* locus from a tetO vector pAS3027. The transformation construct, including upstream and downstream homology, included CaTar-TetO-FlpNAT. This construct was transformed into lab strain Sn152, an auxotrophic derivative of SC5314, by lithium acetate and heat shock transformation. Transformants were screened for correct insertion using PCR for both upstream and downstream flanks of the transformed region. Sanger sequencing was used to determine which allele of *NCP1* was overexpressed. For strains containing both the tetO-*NCP1* and *KSR1* LOH1 constructs, NAT was removed from the tetO-*NCP1* strains by growth on FBS to activate FLP recombinase, and then transformed with the same protocol described above for *KSR1* LOH1.

Construction of *KSR1* deletion mutants in SC5314

The *KSR1* deletion mutants in the SC5314 background were constructed using the CRISPR system developed by [77]. The intact CRISPR cassette was built with plasmids pADH118 for gRNA expression and plasmid pADH99 for Cas9 components. Both plasmids had the carbenicillin selection marker, and when cut and stitched together they reconstituted the NAT marker. The LEUpOUT strategy was used to remove the CRISPR components and the NAT marker. The *C. albicans* strain AHY940 (SC5314 *LEU2* heterozygous knockout) was used to transform and produce the mutants. The parental strain and plasmids were provided by the Hernday lab.

Construction of strains carrying *mNeon-Green-Ksr1p*

To generate *C. albicans* strains with a tagged Ksr1 protein, we amplified: *NAT1* from plasmid pJB-T155 (primers 2313 and 2251), mNeonGreen from plasmid pJB-T409 (primers 2315 and 2369), the plasmid backbone containing an *E. coli* origin of replication, and the Amp^R gene from pJB-T155 (primers 2325 and 2027). The promoter sequence of *TDH3* was amplified from the genomic DNA of *C. albicans* SC5314 (primers 2239 and 2314).

The plasmid expression cassette (*NAT1-TDH3-mNeonGreen*) was amplified from pJB-T510 by PCR using PCRBIO VeriFi™ Mix with primers CB-KSR1-F, CB-KSR1-R, which are complementary to 40 bp 5'-to the start codon of the *KSR1* ORF, and 40 bp downstream of the start codon. The amplified PCR product was used to transform a fresh *C. albicans* SC5314 log phase liquid culture and transformants were selected on YPD + nourseothricin (400 µg/ml).

Successful transformants were validated by diagnostic PCR using PhireGreen Hot Start II PCR Master Mix along with primers specific for the expression cassette and *KSR1* (#2039, #CB-KSR1-CHK). To determine which allele of the gene was fused to mNeonGreen, the sequence

was amplified by PCR (primers #2039, #2342), cleaned using a Qiagen PCR cleaning kit, and Sanger sequenced.

Construction of *KSR1*$^{189R/R}$

To construct the strain with single nucleotide mutation resulting in *KSR1*$^{189R/R}$ genotype, we used the site-specific mutagenesis "LEUpOUT" system [77] customized to target the desired gene and PCRBIO VeriFi™ Mix for PCR. Briefly, fragment "A" has a split NAT gene, fragment "B" contains the gRNA and a *LEU2* homology region, and fragment "C" is made by PCR stitching of fragments "A" + "B".

For making strains homozygous for 189R/R, we used a gRNA and donor DNA fragment amplified by pairs of primers (2902, 2903, S2 Table). Following the annotation in the "LEUpOUT" system, Fragment "A" included the pSNR52 promoter, and a split *NAT1* (part2 of 2) was amplified from plasmid pJB-T482 using primers 2890 and 2891. Fragment "B" had a *LEU2* homologous region and a custom gRNA, that was made using plasmid pJB-T486 and oligos 2898 and 2892 (S2 Table). Fragment "C" was made by stitching together fragments "A" and "B", using primers 2893 and 2895. Plasmid pJB-T487, which contains a split *NAT1* (part1 of 2), the CAS9 expression construct, and a *LEU2* homology region, was digested with restriction enzyme MssI to release this region for use in transformation.

Fragment "C", the digested pJB-T487, and the donor DNA were used to transform *C. albicans* YJBT-2760 strain. Transformants were first selected on YPD + nourseothricin (400 µg/ml), then on SDC lacking leucine. To ask if the targeted sites of *KSR1* were repaired by the donor DNA and carry the designed single nucleotide mutations, the region was amplified by PCR with the PhireGreen Hot Start II PCR Master Mix (primers 2341, 2342), cleaned with a Qiagen PCR

cleaning kit, and sent for Sanger sequencing. Upon whole genome sequencing, we discovered that this mutant did undergo LOH for much of chromosome R (S11 Fig).

Alphafold protein structure predictions

Ribbon models of structural predictions for *KSR1A* and *KSR1B* were generated using *Alphafold* (version 2.3.2) [60]. Protein coding sequences for *KSR1A* and *KSR1B* were downloaded from the Candida Genome Database [78] from the V22 reference genome and submitted for Alphafold predictions using the colab notebook found at: https://colab.research.google.com/github/deepmind/alphafold/blob/main/notebooks/AlphaFold.ipynb, using default parameters.

Fluorescence microscopy of tagged *KSR1* alleles

Cells were picked from an agar plate into SDC medium and grown overnight by incubating at 30°C with shaking. The following day, cells were diluted 1:50 into fresh SDC. For fluorescence microscopy of the mNeonGreen-tagged protein and staining with an endoplasmic reticulum-specific probe 2 [66] the cells were incubated at 30°C for 2 hours with shaking, the stain was added to a final concentration of 1 µM, and the cells were incubated for an additional hour in the dark. 3-5µL of cell culture was deposited on a glass slide topped with 10 µL of low melt agar and imaged with a Nikon Ti Eclipse microscope using the Nikon Elements AR software, and Nikon Plan Apo x100 objective. Filters used were: 488 nm mNeonGreen excitation and 510 nm for emission; for the ER-specific stain CFP 438 nm excitation and 483 nm emission.

Lipid analysis

908 Strains AMS2401, AMS5778, AMS5779, AMS5784, AMS5780, and AMS5782 were grown
909 overnight in 10 ml of SDC at 30°C under agitation. Cell suspensions were centrifuged, washed
910 in sterile PBS and counted. Then, $1x10^8$ cells were inoculated in 10 ml of fresh SDC only, or in
911 media containing 1 or 10 µg/ml of fluconazole and grown for additional 48 h at 30°C. Prior to cell
912 lysis, C17-sphingolipid standards were added to the samples [79,80]. Mandala extraction was
913 carried out as described previously [81], followed by Bligh and Dyer Extraction [82]. A third of
914 each sample obtained from the Bligh and Dyer Extraction was reserved for inorganic phosphate
915 (Pi) determination, so the relative sphingolipid signal was normalized by the Pi abundance. The
916 organic phase was transferred to a new tube and submitted to alkaline hydrolysis of
917 phospholipids [83]. Finally, the organic phase was dried and used for mass spectrometry
918 analysis [80].
919
920 Sphingolipid abundances, normalized by Pi abundance, were then analyzed using R (version
921 4.1.3). Any lipid species that were not detected in any sample were removed from analysis.
922 Because the distribution of lipid abundances was exponential across samples, $\log_{10}$ values were
923 calculated for all normalized abundances, and heatmaps generated using the $\log_{10}$ transformed
924 values. Heatmaps were generated using the R package *pheatmap* (version 1.0.12) [84], and
925 scaled by row (across samples) to result in heatmap color intensities that represent each sample's
926 z-score calculated from the distribution of all samples in the row.
927

928 # RNA sequencing

929 *C. albicans* cells were cultured overnight in liquid YPD medium (2% bacto-peptone, 1% yeast
930 extract, 2% dextrose (filter-sterilized)) at 30°C with shaking (200 rpm) and then diluted 1/50 in
931 YPD either without FLC, with 2 µg/ml FLC, or with 64 µg/ml FLC. After 24 h at 30°C with shaking
932 (200 rpm), 1 ml of the cell suspension was utilized to extract total RNA using the Ribopure-Yeast

RNA kit (AM1926, Invitrogen), according to the manufacturer's instructions. A Bioanalyzer (Agilent) was used for the qualitative sample analysis, and only those with RNA quality (RIN) scores of 7 or higher and a 260/280 ratio within the range of 2.13-2.2 were sequenced. Sequencing was performed with the help of the Biomics Platform at Institut Pasteur using pair-end Illumina stranded-mRNA sequencing. RNA sequences reported in this paper have been deposited in the NCBI Sequence Read Archive, https://www.ncbi.nlm.nih.gov/bioproject (BioProject ID PRJNA1063495).

RNA sequencing data analysis

The paired reads from the RNA-seq libraries were trimmed for low-quality reads, and Illumina TruSeq adapters were removed with Cutadapt v1.9.1 [85] with the following parameters: --trim-qualities 30 -e (maximum error rate) 0.1 --times 3 --overlap 6 --minimum-length 30. The cleaning of rRNA sequences was performed with Bowtie2 v2.3.3 [86] with default parameters. The cleaned reads from RNA-seq paired-end libraries were aligned to the *C. albicans* SC5314 reference genome (Version_A22-s07-m01) with Tophat2 v2.0.14 [87] and the following parameters: minimum intron length 30; minimum intron coverage 30; minimum intron segment 30; maximum intron length 4000; maximum multihits 1; and microexon search. Genes were counted using featureCounts v2.0.0 [88] from the Subreads package (parameters: -t gene -g gene_id -s 2 -p). Analysis of differential expression data was performed in DeSeq2 [89]. The statistical analysis process includes data normalization, graphical exploration of raw and normalized data, tests for differential expression for each feature between the conditions, and raw P-value adjustment. The genes with adjusted P-value less than 0.1 were considered as differentially expressed compared to the non-treated condition (YPD no FLC). Log_2 fold changes for each evolved strain relative to the progenitor strain in no FLC were plotted as heatmaps

using *pheatmap* [84] without any additional scaling, and asterisks were used to denote significant P-values as described above.

Cy5 and R6G flow cytometry

C. albicans cells were grown overnight in liquid YPD medium (1% yeast extract, 2% peptone, and 2% dextrose (with the dextrose filter sterilized)) at 30°C with shaking (200 rpm). Cultures were diluted 1 in 100 in a 3 mL volume of YPD and compounds were added to final concentrations of 1 µg/mL for Rhodamine 6G (Sigma), or 1 µM for FLC-Cy5. Samples incubated with 10 µg/mL of Beauvericin (Sigma) were used as positive controls and those incubated with corresponding volumes of DMSO were used as negative controls. Cells were incubated at 30°C with shaking and harvested after 4 h, washed twice with sterile PBS and diluted to a density of ~10^6 cells/mL in PBS. Fluorescence was measured in 200 µL aliquots of cell suspension and data were collected from 100,000 cells per sample using a Miltenyi MACSQuant Analyzer 10 Flow Cytometer. Cell populations were gated by SSC/FSC to eliminate small debris particles. Experiments were performed with at least three biological and two technical replicates. Analyses were performed using FlowJo 10.8.

Rhodamine 6G efflux assay

C. albicans cells were patched from glycerol stocks onto YPAD agar plates and grown at 30°C for ~1 day. Patches were used to inoculate 3 mL liquid YPAD media with 2% dextrose (20 g/L bactopeptone, 10 g/L yeast extract, 0.04 g/L adenine, 0.08 g/L uridine), and grown at 30°C overnight with shaking. Cultures were then back-diluted, adding 50 µL of overnight culture into 5 mL of fresh media with 0 µg/mL FLC, 1 µg/mL FLC, or 10 µg/mL FLC added at grown for 3 hours at 30°C with shaking. Cultures were spun down and washed with PBS (pH 7, room temperature), and then resuspended in 2 mL PBS and incubated for 2 hours at 30°C with

shaking. Rhodamine 6G (ThermoFisher #419010050) was added to a final concentration of 10 µg/mL and cultures incubated for 1 hour at 30°C with shaking. Cultures were spun down and washed twice with 4°C PBS, and then resuspended in a final volume of 900 µL of PBS. Cultures were then split across 6 wells of a 96-well plate to constitute technical triplicate for a set with and without dextrose (at 150 µL per well). Baseline fluorescence and optical density (OD_{600}) measurements were taken using a BioTrex HTX plate reader (excitation 485 nm, emission 525 nm) for 5 minutes at 1 minute intervals. The plate was then removed, and dextrose was added to the 'with dextrose' samples to a final concentration of 1%. The plate was then returned to the plate reader and fluorescence and OD measurements were taken every 4 min for a total of 90 min. Three biological replicates were performed.

Fluorescent imaging of lipid droplets

C. albicans cells were cultured in liquid YPD medium (2% bacto-peptone, 1% yeast extract, 2% dextrose (filter-sterilized)) overnight at 30°C with continuous shaking (200 rpm). The number of cells was determined by measuring optical densities (OD_{600}) using a Biotek Epoch 2 plate reader. 106 cells/mL were resuspended in YPD in different conditions: no drug, with 128 µg/ml Fluconazole (FLC, PHR1160-1G, Sigma Aldrich), or with 128 µg/ml myriocin (MYO, M1177-5M, Sigma Aldrich). The cell suspensions were incubated for 3 h at 30°C (200 rpm). After incubation, cells were washed twice with sterile PBS and incubated with 1 µg/ml Bodipy 493/503 (D3922, Invitrogen) for 10 minutes at 30°C and 200 rpm. The cell suspension was washed twice with sterile PBS. The cells were then imaged at a 60X magnification with a GFP filter and an exposure of 125 ms on a Zeiss AxioVision Rel. 4.8 microscope. Cellprofiler4.2.6 (https://cellprofiler.org/, available at https://github.com/CellProfiler/CellProfiler) was used to analyze the images. The Speckle Counting pipeline (https://cellprofiler.org/examples) was used to identify smaller objects within larger ones and to establish a relationship between them.

Objects with a diameter of 30-100 pixels were considered as yeast cells, while those with a diameter of 1-6 pixels were classified as lipid bodies. The same pipeline was used to quantify several parameters. These include the number of lipid bodies within each cell, the highest pixel intensity within each lipid body (referred to as maximum brightness), and the integrated intensity of lipid bodies. The integrated intensity was quantified by summing the pixel intensities within these structures. All assays were performed with biological triplicates, with at least 200 cells analyzed per replicate.

Fluorescent imaging of vacuoles

C. albicans cells were cultured in liquid YPD medium (2% bacto-peptone, 1% yeast extract, 2% dextrose (filter-sterilized)) overnight at 30°C with shaking (200 rpm) and resuspended in YPD or YPD + FLC (128 µg/ml) at a concentration of 106 cells/mL. To stain the vacuoles, cells were incubated with 8 µM of SynaptoRed C2 (S6689, Sigma) for 3 h at 30°C with shaking. The cell suspension was then washed with 1 mL of fresh YPD and transferred to 4 mL of YPD before incubating for 90 min at 30°C (200 rpm). The cells were washed with sterile PBS before imaging at a 60X magnification with an mCherry filter and an exposure of 100 ms on a Zeiss AxioVision Rel. 4.8 microscope. Cellprofiler4.2.6 (https://cellprofiler.org/, available at https://github.com/CellProfiler/CellProfiler) was used to analyze the images. The Speckle Counting pipeline (https://cellprofiler.org/examples) was used to identify objects with diameters of 10-35 pixels, these objects were considered as vacuoles. The sum of the pixel intensities within these vacuoles, represented by the integrated intensity, and the area of these vacuoles were quantified using Speckle Counting. All assays were performed with biological triplicates, with at least 200 cells analyzed for each replicate.

RT-qPCR

C. albicans cells were patched onto solid YPAD agar from frozen glycerol stocks and grown at 30°C for ~2 days. Patches were used to inoculate 3 mL YPAD media (2% dextrose) and grown overnight at 30°C with shaking. 350 µL of overnight cultures were back diluted into 50mL fresh YPAD media with 0 µg/mL FLC or 1 µg/mL FLC added, and grown at 30°C with shaking until cultures reached an OD between 0.4-0.5. 5 mL of each culture was pelleted, supernatant removed, and cell pellets flash frozen in liquid nitrogen, and then stored at -80°C until RNA could be harvested. RNA was extracted using the Qiagen RNeasy Mini Kit (CAT# 74106), using the mechanical disruption method with a Omni International Bead Ruptor Elite. 1 ug of RNA from each sample was DNase treated after elution, via incubation with DNase at 37°C for 30 min followed by the addition of EDTA to a final concentration of 5mM and heat inactivation at 75°C for 5 min. cDNA was prepared using SuperScript II RT (ThermoFisher, Cat# 18064014) using an Oligo(dT) primer according to the manufacturer's recommendations. cDNA was used as template for qPCR reactions performed in technical triplicate with primers specific to either *TEF1*, *ACT1*, or *CDR1* for each sample as well as noRT and no template controls, using PowerUp SYBR Green Mastermix (Fisher Scientific, CAT# A25742) run on a BioRad CFX-96. Delta-delta Ct values for *CDR1* were calculated, with propagation of error, relative to either *TEF1* or *ACT1* and then relative to the progenitor strain in 0 µg/mL FLC. Three complete biological replicates were performed.

Spot plates

C. albicans cells were patched onto solid YPAD agar plates and grown at 30°C for ~2 days. Patches were used to inoculate 3 mL of liquid YPAD media (2% dextrose) and grown overnight at 30°C with shaking. Cultures were diluted to ~10^7 cells/mL in PBS and serial dilutions performed to generate suspensions at 10^6, 10^5, 10^4, and 10^3 cells/mL. 5 µL of each suspension

was spotted onto YPAD agar plates with 0% or 0.02% sodium dodecyl sulfate. Cells were incubated at 30°C and pictures taken at 24 and 48 hours.

Filamentation assays

C. albicans cells were cultured in liquid YPD medium (2% bacto-peptone, 1% yeast extract, 2% dextrose (filter-sterilized)) overnight at 30°C with shaking (200 rpm). Yeast cells were diluted 1/50 in 4 ml of YPD and seeded in 6-well plates. After 2 h at 37°C with shaking (200 rpm), the cell suspension was then washed twice with sterile PBS and imaged at a 60X magnification in brightfield on a Zeiss AxioVision Rel. 4.8 microscope. All assays were performed with three biological replicates, with at least 200 cells analyzed for each replicate. Representative images are shown in the Figs.

Galleria mellonella infections

G. mellonella larvae were sourced from La ferme aux Coleos (Cherbourg-en-Cotentin, France), maintained at room temperature, and were used within one week of delivery. Larvae without any signs of melanization and with an average weight of 0.4 g were selected for each experiment in groups of 12. *C. albicans* cells were cultured in liquid YPD medium (2% bacto-peptone, 1% yeast extract, 2% dextrose, filter-sterilized). Following an overnight incubation at 30°C with shaking (200 rpm), cells were washed twice with sterile PBS. The cell concentrations were then determined using a Luna FX7 Automatic Cell Counter (Logos Biosystems) and adjusted to 3×10^7 cells/mL in sterile PBS. For the infection, each larva was injected with 3×10^5 cells/mL through the last left pro-leg using a 10 µL glass syringe and a 26S gauge needle (Hamilton, 80300). A subsequent injection with either fluconazole (0.2 µg/larva) or a sterile vehicle (PBS at matching injection volumes) was administered via the last right pro-leg, 2 h post-infection. The inoculum size was verified by plating fungal cells on YPD and counting the resulting colony forming units (CFUs).

Both infected and control groups of larvae were maintained at 37 °C for 14 days, with daily monitoring of survival. Larvae were deemed dead if no movement was observed upon contact. The experiments were conducted with three biological replicates. Control groups of larvae included those treated with PBS or FLC without fungal infection.

Mouse survival study

Male CD-1 mice were inoculated via the tail vein with 2 x 10^5 cells of *C. albicans*, using 5 mice per strain. The mice were monitored twice daily for survival by an observer who was blinded to the identity of the infecting strain. Mice that showed signs of substantial distress were humanely euthanized.

Ethics statement

The mouse studies were approved by the Institutional Animal Care and Use Committee at the Lundquist Institute for Biomedical Innovation at Harbor-UCLA Medical Center.

Acknowledgements

We are grateful to lab members Robert T. Todd (UMN), Naomi Ziv (TAU), and Cristina Avila (TAU) for technical support. We thank Chen Bibi for constructing plasmid pJB-T510, and Dr. Anna Dukhovney for assisting with microscopy imaging.

Conflicts of Interest

Dr. Maurizio Del Poeta, M.D., is a Co-Founder and Chief Scientific Officer (CSO) of MicroRid Technologies Inc. The goal of MicroRid Technologies Inc. is to develop new anti-fungal agents of therapeutic use. All other authors declare no competing interests.

References

1. Cowen LE, Sanglard D, Howard SJ, Rogers PD, Perlin DS. Mechanisms of Antifungal Drug Resistance. Cold Spring Harb Perspect Med. 2014;5: a019752–a019752.

2. Franz R, Kelly SL, Lamb DC, Kelly DE, Ruhnke M, Morschhäuser J. Multiple molecular mechanisms contribute to a stepwise development of fluconazole resistance in clinical Candida albicans strains. Antimicrob Agents Chemother. 1998;42: 3065–3072.

3. Sasse C, Dunkel N, Schäfer T, Schneider S, Dierolf F, Ohlsen K, et al. The stepwise acquisition of fluconazole resistance mutations causes a gradual loss of fitness in Candida albicans. Mol Microbiol. 2012;86: 539–556.

4. Flowers SA, Colón B, Whaley SG, Schuler MA, Rogers PD. Contribution of clinically derived mutations in ERG11 to azole resistance in Candida albicans. Antimicrob Agents Chemother. 2015;59: 450–460.

5. Dutta A, Dutreux F, Schacherer J. Loss of heterozygosity spectrum depends on ploidy level in natural yeast populations. Mol Biol Evol. 2022. doi:10.1093/molbev/msac214

6. Sharp NP, Sandell L, James CG, Otto SP. The genome-wide rate and spectrum of spontaneous mutations differ between haploid and diploid yeast. Proc Natl Acad Sci U S A. 2018;115: E5046–E5055.

7. Zhu YO, Siegal ML, Hall DW, Petrov DA. Precise estimates of mutation rate and spectrum in yeast. Proceedings of the National Academy of Sciences. 2014;111: E2310–E2318.

8. Ene IV, Farrer RA, Hirakawa MP, Agwamba K, Cuomo CA, Bennett RJ. Global analysis of mutations driving microevolution of a heterozygous diploid fungal pathogen. Proc Natl Acad Sci U S A. 2018;115: E8688–E8697.

9. White TC. The presence of an R467K amino acid substitution and loss of allelic variation correlate with an azole-resistant lanosterol 14alpha demethylase in Candida albicans. Antimicrob Agents Chemother. 1997;41: 1488–1494.

10. Xiang M-J, Liu J-Y, Ni P-H, Wang S, Shi C, Wei B, et al. Erg11 mutations associated with azole resistance in clinical isolates of Candida albicans. FEMS Yeast Res. 2013;13: 386–393.

11. Flowers SA, Barker KS, Berkow EL, Toner G, Chadwick SG, Gygax SE, et al. Gain-of-function mutations in UPC2 are a frequent cause of ERG11 upregulation in azole-resistant clinical isolates of Candida albicans. Eukaryot Cell. 2012;11: 1289–1299.

12. Selmecki A, Gerami-Nejad M, Paulson C, Forche A, Berman J. An isochromosome confers drug resistance in vivo by amplification of two genes, ERG11 and TAC1. Mol Microbiol. 2008;68: 624–641.

13. Silver PM, Oliver BG, White TC. Role of Candida albicans transcription factor Upc2p in drug resistance and sterol metabolism. Eukaryot Cell. 2004;3: 1391–1397.

14. MacPherson S, Akache B, Weber S, De Deken X, Raymond M, Turcotte B. Candida albicans zinc cluster protein Upc2p confers resistance to antifungal drugs and is an activator of ergosterol biosynthetic genes. Antimicrob Agents Chemother. 2005;49: 1745–1752.

15. Sanglard D, Ischer F, Parkinson T, Falconer D, Bille J. Candida albicans mutations in the ergosterol biosynthetic pathway and resistance to several antifungal agents. Antimicrob Agents Chemother. 2003;47: 2404–2412.

16. Ksiezopolska E, Schikora-Tamarit MÀ, Beyer R, Nunez-Rodriguez JC, Schüller C, Gabaldón T. Narrow mutational signatures drive acquisition of multidrug resistance in the fungal pathogen Candida glabrata. Curr Biol. 2021;31: 5314-5326.e10.

17. Scott NE, Edwin Erayil S, Kline SE, Selmecki A. Rapid Evolution of Multidrug Resistance in a Candida lusitaniae Infection during Micafungin Monotherapy. Antimicrob Agents Chemother. 2023;67: e0054323.

18. Prasad R, Rawal MK, Shah AH. Candida Efflux ATPases and Antiporters in Clinical Drug Resistance. Adv Exp Med Biol. 2016;892: 351–376.

19. Coste AT, Karababa M, Ischer F, Bille J, Sanglard D. TAC1, transcriptional activator of CDR genes, is a new transcription factor involved in the regulation of Candida albicans ABC transporters CDR1 and CDR2. Eukaryot Cell. 2004;3: 1639–1652.

20. Perea S, López-Ribot JL, Kirkpatrick WR, McAtee RK, Santillán RA, Martínez M, et al. Prevalence of molecular mechanisms of resistance to azole antifungal agents in Candida albicans strains displaying high-level fluconazole resistance isolated from human immunodeficiency virus-infected patients. Antimicrob Agents Chemother. 2001;45: 2676–2684.

21. Berman J, Krysan DJ. Drug resistance and tolerance in fungi. Nat Rev Microbiol. 2020;18: 319–331.

22. Martin SW, Konopka JB. Lipid raft polarization contributes to hyphal growth in Candida albicans. Eukaryot Cell. 2004;3: 675–684.

23. Pasrija R, Panwar SL, Prasad R. Multidrug transporters CaCdr1p and CaMdr1p of Candida albicans display different lipid specificities: both ergosterol and sphingolipids are essential for targeting of CaCdr1p to membrane rafts. Antimicrob Agents Chemother. 2008;52: 694–704.

24. Song J, Liu X, Li R. Sphingolipids: Regulators of azole drug resistance and fungal pathogenicity. Mol Microbiol. 2020;114: 891–905.

25. Arendrup MC, Cuenca-Estrella M, Lass-Flörl C, Hope W, EUCAST-AFST. EUCAST technical note on the EUCAST definitive document EDef 7.2: method for the determination of broth dilution minimum inhibitory concentrations of antifungal agents for yeasts EDef 7.2 (EUCAST-AFST). Clin Microbiol Infect. 2012;18: E246-7.

26. Rosenberg A, Ene IV, Bibi M, Zakin S, Segal ES, Ziv N, et al. Antifungal tolerance is a subpopulation effect distinct from resistance and is associated with persistent candidemia. Nat Commun. 2018;9: 2470.

27. Levinson T, Dahan A, Novikov A, Paran Y, Berman J, Ben-Ami R. Impact of tolerance to fluconazole on treatment response in Candida albicans bloodstream infection. Mycoses. 2021;64: 78–85.

28. Rueda C, Puig-Asensio M, Guinea J, Almirante B, Cuenca-Estrella M, Zaragoza O, et al. Evaluation of the possible influence of trailing and paradoxical effects on the clinical outcome of patients with candidemia. Clin Microbiol Infect. 2017;23: 49.e1-49.e8.

29. Astvad KMT, Sanglard D, Delarze E, Hare RK, Arendrup MC. Implications of the EUCAST Trailing Phenomenon in Candida tropicalis for the In Vivo Susceptibility in Invertebrate and Murine Models. Antimicrob Agents Chemother. 2018;62. doi:10.1128/AAC.01624-18

30. Gao J, Wang H, Li Z, Wong AH-H, Wang Y-Z, Guo Y, et al. Candida albicans gains azole resistance by altering sphingolipid composition. Nat Commun. 2018;9: 4495.

31. Delarze E, Brandt L, Trachsel E, Patxot M, Pralong C, Maranzano F, et al. Identification and Characterization of Mediators of Fluconazole Tolerance in Candida albicans. Front Microbiol. 2020;11: 591140.

32. Vandenbosch D, Bink A, Govaert G, Cammue BPA, Nelis HJ, Thevissen K, et al. Phytosphingosine-1-phosphate is a signaling molecule involved in miconazole resistance in sessile Candida albicans cells. Antimicrob Agents Chemother. 2012;56: 2290–2294.

33. Wang H, Ji Z, Feng Y, Yan T, Cao Y, Lu H, et al. Myriocin enhances the antifungal activity of fluconazole by blocking the membrane localization of the efflux pump Cdr1. Front Pharmacol. 2022;13: 1101553.

34. Rollin-Pinheiro R, Bayona-Pacheco B, Domingos LTS, da Rocha Curvelo JA, de Castro GMM, Barreto-Bergter E, et al. Sphingolipid Inhibitors as an Alternative to Treat Candidiasis Caused by Fluconazole-Resistant Strains. Pathogens. 2021;10. doi:10.3390/pathogens10070856

35. Revie NM, Iyer KR, Maxson ME, Zhang J, Yan S, Fernandes CM, et al. Targeting fungal membrane homeostasis with imidazopyrazoindoles impairs azole resistance and biofilm formation. Nat Commun. 2022;13: 3634.

36. Puumala E, Zaslaver O, Chen A, Duncan D, Fogal M, Shapiro RS, et al. The Trisubstituted Isoxazole MMV688766 Exerts Broad-Spectrum Activity against Drug-Resistant Fungal Pathogens through Inhibition of Lipid Homeostasis. MBio. 2022;13: e0273022.

37. Fornarotto M, Xiao L, Hou Y, Koch KA, Chang E, O'Malley RM, et al. Sphingolipid biosynthesis in pathogenic fungi: identification and characterization of the 3-

ketosphinganine reductase activity of Candida albicans and Aspergillus fumigatus. Biochim Biophys Acta. 2006;1761: 52–63.

38. Bougnoux M-E, Pujol C, Diogo D, Bouchier C, Soll DR, d'Enfert C. Mating is rare within as well as between clades of the human pathogen Candida albicans. Fungal Genet Biol. 2008;45: 221–231.

39. Muzzey D, Schwartz K, Weissman JS, Sherlock G. Assembly of a phased diploid Candida albicans genome facilitates allele-specific measurements and provides a simple model for repeat and indel structure. Genome Biol. 2013;14: R97.

40. Marton T, Feri A, Commere P-H, Maufrais C, d'Enfert C, Legrand M. Identification of Recessive Lethal Alleles in the Diploid Genome of a Candida albicans Laboratory Strain Unveils a Potential Role of Repetitive Sequences in Buffering Their Deleterious Impact. mSphere. 2019;4. doi:10.1128/mSphere.00709-18

41. Liang S-H, Bennett RJ. The Impact of Gene Dosage and Heterozygosity on The Diploid Pathobiont Candida albicans. J Fungi (Basel). 2019;6. doi:10.3390/jof6010010

42. Bennett RJ, Forche A, Berman J. Rapid Mechanisms for Generating Genome Diversity: Whole Ploidy Shifts, Aneuploidy, and Loss of Heterozygosity. Cold Spring Harb Perspect Med. 2014;4. doi:10.1101/cshperspect.a019604

43. Gerstein AC, Kuzmin A, Otto SP. Loss-of-heterozygosity facilitates passage through Haldane's sieve for Saccharomyces cerevisiae undergoing adaptation. Nat Commun. 2014;5: 3819.

44. Forche A, Abbey D, Pisithkul T, Weinzierl MA, Ringstrom T, Bruck D, et al. Stress alters rates and types of loss of heterozygosity in Candida albicans. MBio. 2011;2. doi:10.1128/mBio.00129-11

45. Forche A. Large-Scale Chromosomal Changes and Associated Fitness Consequences in Pathogenic Fungi. Curr Fungal Infect Rep. 2014;8: 163–170.

46. Yang F, Scopel EFC, Li H, Sun L-L, Kawar N, Cao Y-B, et al. Antifungal Tolerance and Resistance Emerge at Distinct Drug Concentrations and Rely upon Different Aneuploid Chromosomes. MBio. 2023; e0022723.

47. Todd RT, Soisangwan N, Peters S, Kemp B, Crooks T, Gerstein A, et al. Antifungal drug concentration impacts the spectrum of adaptive mutations in Candida albicans. Mol Biol Evol. 2023. doi:10.1093/molbev/msad009

48. Vande Zande P, Zhou X, Selmecki A. The Dynamic Fungal Genome: Polyploidy, Aneuploidy and Copy Number Variation in Response to Stress. Annu Rev Microbiol. 2023. doi:10.1146/annurev-micro-041320-112443

49. Selmecki A, Forche A, Berman J. Aneuploidy and isochromosome formation in drug-resistant Candida albicans. Science. 2006;313: 367–370.

50. Todd RT, Wikoff TD, Forche A, Selmecki A. Genome plasticity in Candida albicans is driven by long repeat sequences. Elife. 2019;8. doi:10.7554/eLife.45954

1252 51. Todd RT, Selmecki A. Expandable and reversible copy number amplification drives rapid
1253 adaptation to antifungal drugs. Verstrepen KJ, Wittkopp PJ, editors. Elife. 2020;9: e58349.

1254 52. Giaever G, Chu AM, Ni L, Connelly C, Riles L, Véronneau S, et al. Functional profiling of
1255 the Saccharomyces cerevisiae genome. Nature. 2002;418: 387–391.

1256 53. Beeler T, Bacikova D, Gable K, Hopkins L, Johnson C, Slife H, et al. The Saccharomyces
1257 cerevisiae TSC10/YBR265w gene encoding 3-ketosphinganine reductase is identified in a
1258 screen for temperature-sensitive suppressors of the Ca2+-sensitive csg2Delta mutant. J
1259 Biol Chem. 1998;273: 30688–30694.

1260 54. Zhao P, Zhuang Z, Guan X, Yang J, Wang W, Kuang Z. Crystal structure of the 3-
1261 ketodihydrosphingosine reductase TSC10 from Cryptococcus neoformans. Biochem
1262 Biophys Res Commun. 2023;670: 73–78.

1263 55. Benhamou RI, Bibi M, Steinbuch KB, Engel H, Levin M, Roichman Y, et al. Real-Time
1264 Imaging of the Azole Class of Antifungal Drugs in Live Candida Cells. ACS Chem Biol.
1265 2017;12: 1769–1777.

1266 56. Maesaki S, Marichal P, Vanden Bossche H, Sanglard D, Kohno S. Rhodamine 6G efflux for
1267 the detection of CDR1-overexpressing azole-resistant Candida albicans strains. J
1268 Antimicrob Chemother. 1999;44: 27–31.

1269 57. Hwang S, Gustafsson HT, O'Sullivan C, Bisceglia G, Huang X, Klose C, et al. Serine-
1270 Dependent Sphingolipid Synthesis Is a Metabolic Liability of Aneuploid Cells. Cell Rep.
1271 2017;21: 3807–3818.

1272 58. Rogers B, Decottignies A, Kolaczkowski M, Carvajal E, Balzi E, Goffeau A. The pleitropic
1273 drug ABC transporters from Saccharomyces cerevisiae. J Mol Microbiol Biotechnol. 2001;3:
1274 207–214.

1275 59. Jarc E, Petan T. Lipid Droplets and the Management of Cellular Stress. Yale J Biol Med.
1276 2019;92: 435–452.

1277 60. Jumper J, Evans R, Pritzel A, Green T, Figurnov M, Ronneberger O, et al. Highly accurate
1278 protein structure prediction with AlphaFold. Nature. 2021;596: 583–589.

1279 61. Varadi M, Anyango S, Deshpande M, Nair S, Natassia C, Yordanova G, et al. AlphaFold
1280 Protein Structure Database: massively expanding the structural coverage of protein-
1281 sequence space with high-accuracy models. Nucleic Acids Res. 2022;50: D439–D444.

1282 62. Benhamou RI, Jaber QZ, Herzog IM, Roichman Y, Fridman M. Fluorescent Tracking of the
1283 Endoplasmic Reticulum in Live Pathogenic Fungal Cells. ACS Chem Biol. 2018;13: 3325–
1284 3332.

1285 63. Xu D, Jiang B, Ketela T, Lemieux S, Veillette K, Martel N, et al. Genome-wide fitness test
1286 and mechanism-of-action studies of inhibitory compounds in Candida albicans. PLoS
1287 Pathog. 2007;3: e92.

1288 64. Garbe E, Gerwien F, Driesch D, Müller T, Böttcher B, Gräler M, et al. Systematic Metabolic
1289 Profiling Identifies De Novo Sphingolipid Synthesis as Hypha Associated and Essential for
1290 Candida albicans Filamentation. mSystems. 2022;7: e0053922.

65. Noble SM, French S, Kohn LA, Chen V, Johnson AD. Systematic screens of a Candida albicans homozygous deletion library decouple morphogenetic switching and pathogenicity. Nat Genet. 2010;42: 590–598.

66. Muller HJ. THE RELATION OF RECOMBINATION TO MUTATIONAL ADVANCE. Mutat Res. 1964;106: 2–9.

67. Sprouffske K, Wagner A. Growthcurver: an R package for obtaining interpretable metrics from microbial growth curves. BMC Bioinformatics. 2016;17: 172.

68. Bolger AM, Lohse M, Usadel B. Trimmomatic: a flexible trimmer for Illumina sequence data. Bioinformatics. 2014;30: 2114–2120.

69. Li H. Aligning sequence reads, clone sequences and assembly contigs with BWA-MEM. arXiv [q-bio.GN]. 2013. Available: http://arxiv.org/abs/1303.3997

70. Li H, Handsaker B, Wysoker A, Fennell T, Ruan J, Homer N, et al. The Sequence Alignment/Map format and SAMtools. Bioinformatics. 2009;25: 2078–2079.

71. McKenna A, Hanna M, Banks E, Sivachenko A, Cibulskis K, Kernytsky A, et al. The Genome Analysis Toolkit: a MapReduce framework for analyzing next-generation DNA sequencing data. Genome Res. 2010;20: 1297–1303.

72. Robinson JT, Thorvaldsdóttir H, Winckler W, Guttman M, Lander ES, Getz G, et al. Integrative genomics viewer. Nat Biotechnol. 2011;29: 24–26.

73. Poplin R, Ruano-Rubio V, DePristo MA, Fennell TJ, Carneiro MO, Van der Auwera GA, et al. Scaling accurate genetic variant discovery to tens of thousands of samples. bioRxiv. 2018. p. 201178. doi:10.1101/201178

74. Ushey K. RcppRoll: Efficient Rolling / Windowed Operations. 2018. Available: https://CRAN.R-project.org/package=RcppRoll

75. Abbey DA, Funt J, Lurie-Weinberger MN, Thompson DA, Regev A, Myers CL, et al. YMAP: a pipeline for visualization of copy number variation and loss of heterozygosity in eukaryotic pathogens. Genome Med. 2014;6: 100.

76. Nguyen N, Quail MMF, Hernday AD. An Efficient, Rapid, and Recyclable System for CRISPR-Mediated Genome Editing in Candida albicans. mSphere. 2017;2. doi:10.1128/mSphereDirect.00149-17

77. Skrzypek MS, Binkley J, Binkley G, Miyasato SR, Simison M, Sherlock G. The Candida Genome Database (CGD): incorporation of Assembly 22, systematic identifiers and visualization of high throughput sequencing data. Nucleic Acids Res. 2017;45: D592–D596.

78. Singh A, Del Poeta M. Sphingolipidomics: An Important Mechanistic Tool for Studying Fungal Pathogens. Front Microbiol. 2016;7: 501.

79. Singh A, MacKenzie A, Girnun G, Del Poeta M. Analysis of sphingolipids, sterols, and phospholipids in human pathogenic Cryptococcus strains. J Lipid Res. 2017;58: 2017–2036.

80. Suzanne M. Mandala, Rosemary A. Thornton, Beth R. Frommer, James E. Curotto, Walter Rozdilsky, Myra B. Kurtz, Robert A. Giacobbe, Gerald F. Bills, M. Angeles Cabello, Isabel Martin, Fernando Pelaez, Guy H. Harris. The Discovery of Australifungin, a Novel Inhibitor of Sphinganine N-Acyltransferase from Sporormiella australis. J Antibiot. 1995;48: 349–356.

81. Bligh EG, Dyer WJ. A RAPID METHOD OF TOTAL LIPID EXTRACTION AND PURIFICATION. Can J Biochem Physiol. 1959;37: 911–917.

82. Clarke NG, Dawson RM. Alkaline O leads to N-transacylation. A new method for the quantitative deacylation of phospholipids. Biochem J. 1981;195: 301–306.

83. Kolde R. pheatmap: Pretty Heatmaps. R package version 1.0. 12. 2019.

84. Martin M. Cutadapt removes adapter sequences from high-throughput sequencing reads. EMBnet.journal. 2011;17: 10–12.

85. Langmead B, Trapnell C, Pop M, Salzberg SL. Ultrafast and memory-efficient alignment of short DNA sequences to the human genome. Genome Biol. 2009;10: R25.

86. Kim D, Pertea G, Trapnell C, Pimentel H, Kelley R, Salzberg SL. TopHat2: accurate alignment of transcriptomes in the presence of insertions, deletions and gene fusions. Genome Biol. 2013;14: R36.

87. Liao Y, Smyth GK, Shi W. featureCounts: an efficient general purpose program for assigning sequence reads to genomic features. Bioinformatics. 2014;30: 923–930.

88. Love MI, Huber W, Anders S. Moderated estimation of fold change and dispersion for RNA-seq data with DESeq2. Genome Biol. 2014;15: 550.

89. Ren J, Hannun YA. Metabolism and Roles of Sphingolipids in Yeast Saccharomyces cerevisiae. In: Geiger O, editor. Biogenesis of Fatty Acids, Lipids and Membranes. Cham: Springer International Publishing; 2017. pp. 1–21.

Supporting information

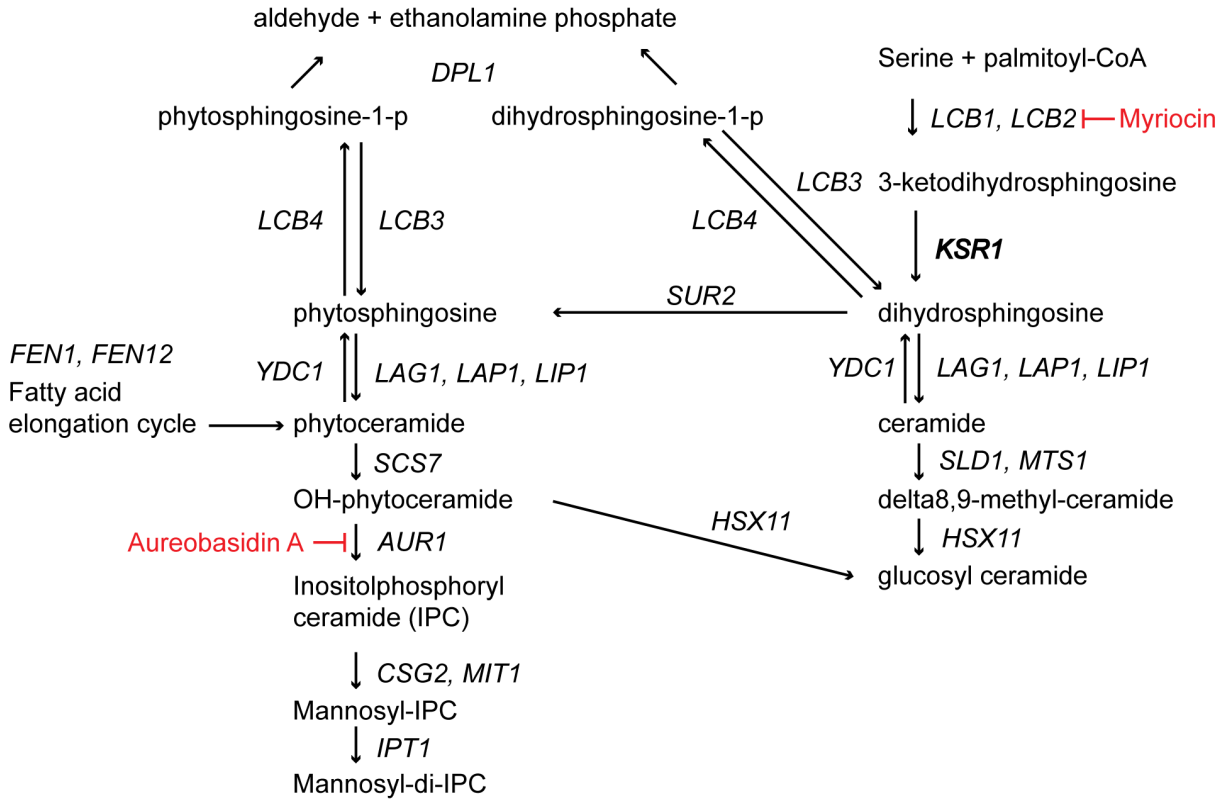

Fig S1. The sphingolipid biosynthesis pathway in *C. albicans*. A flow chart showing the sphingolipid biosynthesis pathway in *C. albicans*, compiled from [30,32,35,67]. Chemical inhibitors are shown in red.

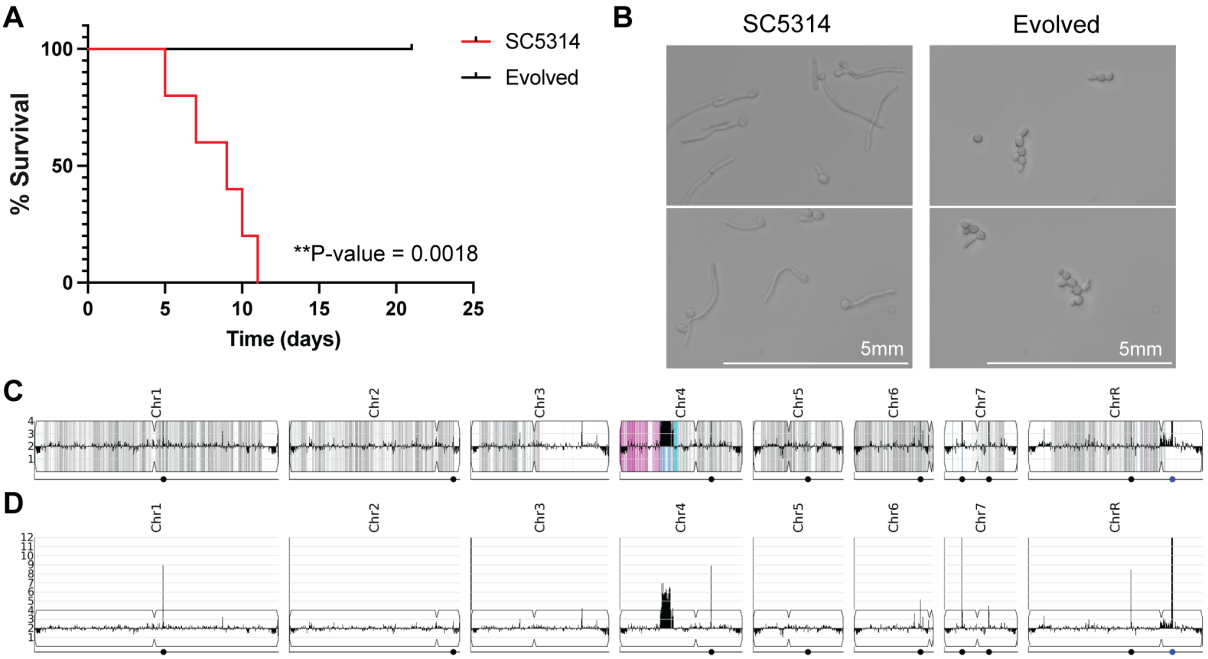

Fig S2. Properties of the evolved population. (A) Survival curves for mice infected with the progenitor strain SC5314 (red) or with the evolved P10 population (black, AMS4058) (Mantel-Cox log-rank test p-value = 0.0018). (B) Representative microscopy images show differences in hyphal formation between the progenitor strain SC5314 (left) and the evolved population (right) after incubation at 37°C for 2 h in rich media. (C) Read depth from whole genome sequencing normalized to average depth across the whole genome is shown for the evolved population, capped at an estimated 4 copies. Colors indicate changes in allele frequencies at heterozygous positions. Blue indicates an increase in the proportion of the “A” reference allele, while pink indicates an increase in the proportion of the “B” reference allele, signifying losses of heterozygosity. (D) Read depth from whole genome sequencing normalized to average depth across the whole genome is shown for the evolved population without a limit to the read depth for the full visualization of the CNV on Chr4. (C and D) Dots indicate positions of major repeat sequences. Blue dot indicates rDNA repeats.

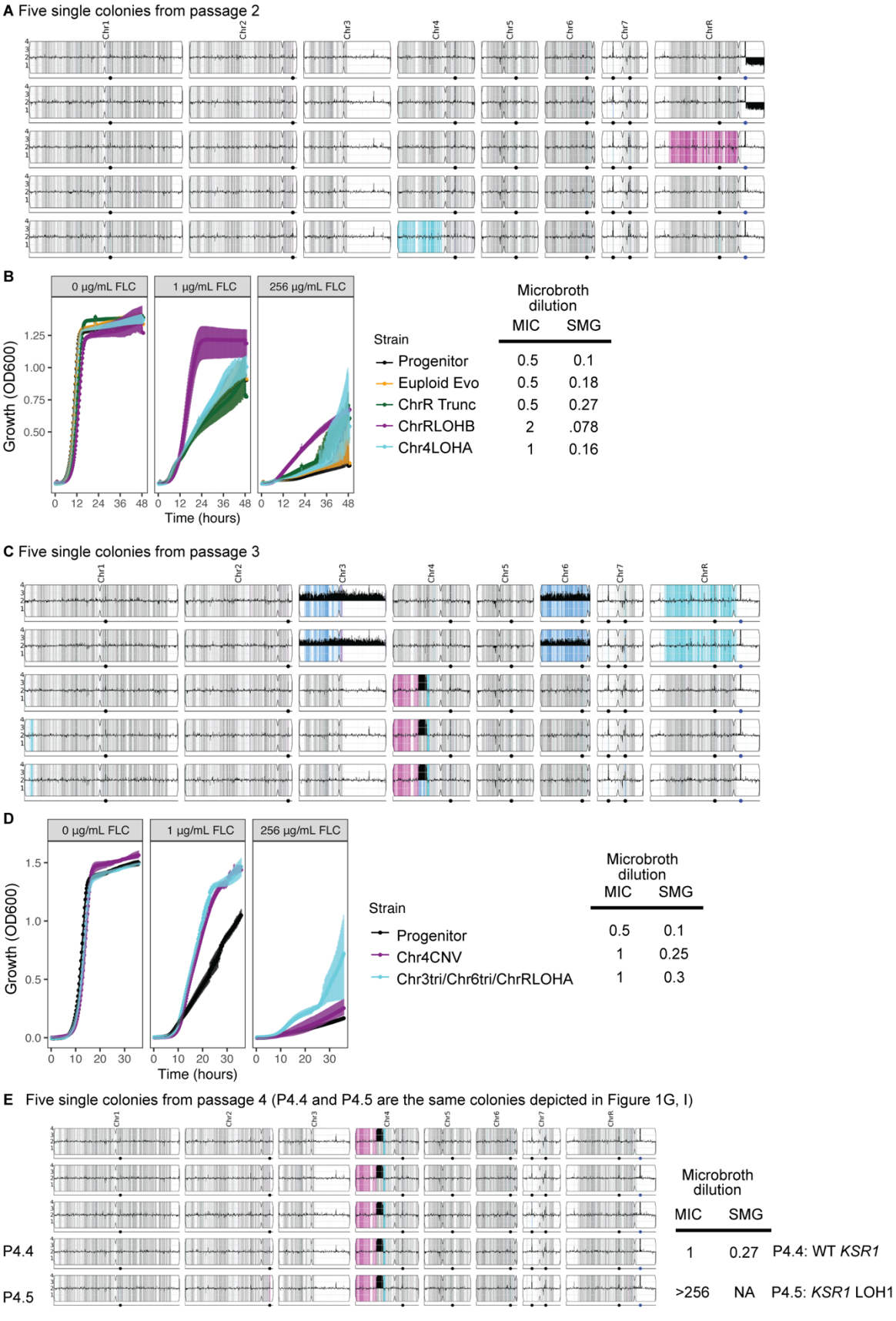

1375

Fig S3. Single colonies isolated from passages 2, 3, and 4. (A) Read depth from whole genome sequencing normalized to average depth across the whole genome is shown for 5 single colonies selected from passage 2 of the evolution experiment. Colors indicate changes in allele frequencies at heterozygous positions. Blue indicates an increase in the proportion of the "A" reference allele, while pink indicates an increase in the proportion of the "B" reference allele, signifying losses of heterozygosity. (B) OD_{600} values for liquid culture growth assays are plotted over time for the wild-type progenitor (black), and the four unique genotypes recovered from passage 2. Growth in rich media without drug, with 1 µg/mL or 256 µg/mL FLC are shown. Error bars are standard errors for three replicates. Tables on the right side indicate average MIC_{50} and SMG values for these genotypes. (C) Read depth plotted as in (A) for five single colonies selected from passage 3 of the evolution experiment. (D) OD values for liquid culture growth assays are plotted over time for the wild-type progenitor (black), and the two unique genotypes recovered from passage 3. Growth in rich media alone or with 1 µg/mL FLC or 256 µg/mL FLC are shown. Error bars are standard errors for three replicates. Tables on the right side indicate average MIC_{50} and SMG values for individual genotypes. (E) Read depth plotted as in (A) for the two unique genotypes from 5 single colonies selected from passage 4 of the evolution experiment.

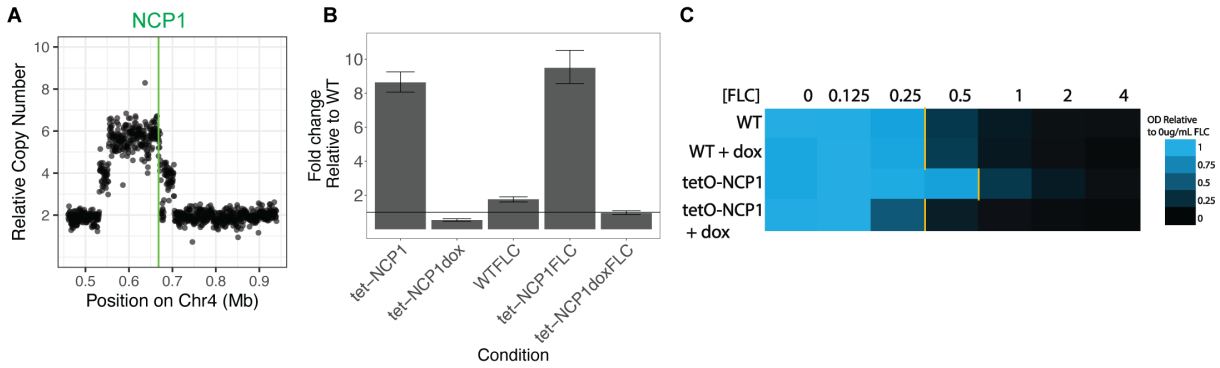

1394

1395 **Fig S4. Overexpression of *NCP1* leads to an increase in MIC_{50}.** (A) Estimated copy number,
1396 calculated as read depth normalized to the rest of the nuclear genome, is plotted for 500 bp
1397 windows across the left arm of chromosome 4. The position of the *NCP1* gene is indicated in
1398 green. (B) RT-qPCR data show fold change in expression of *NCP1* relative to the wild type
1399 background strain. Fold changes are shown for the strain containing the tet-off *NCP1* system in
1400 YPAD without and with doxycycline, and for the wild type strain (WT) and tet-off *NCP1* strain
1401 grown in 1 μg/mL FLC with and without doxycycline. Black line indicates a fold change of 1 (no
1402 change) relative to the wild type strain. Error bars are propagated standard error of three
1403 replicates. (C) A heatmap showing relative growth after 24 hours for the progenitor strain and a
1404 strain containing the native *NCP1* gene under the control of a tet-off promoter system in the
1405 absence (*NCP1* on) and presence of doxycycline (*NCP1* off). Yellow lines indicate MIC_{50} values.
1406

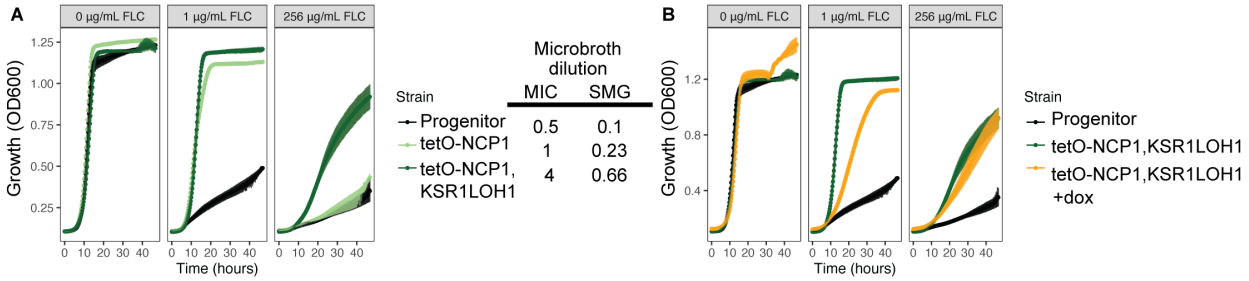

1407

1408 **Fig S5. Combined effect of *NCP1* overexpression and *KSR1* LOH1.**

1409 (A) OD_{600} values for liquid culture growth assays are plotted over time for the wild type

1410 progenitor (black), a strain engineered to contain a tet-off-NCP1 allele (light green) and a strain

1411 engineered to contain both the tet-off-NCP1 allele and the *KSR1* LOH1 (dark green). Growth in

1412 rich media without drug, 1 µg/mL FLC, or 256 µg/mL FLC are shown. Error bars are standard

1413 error for three replicates. MIC_{50} and SMG values calculated at 24 and 48 hours are shown to the

1414 left (see Methods). (B) As in (A), OD values for liquid culture growth assays are plotted over

1415 time for the wild type progenitor (black), a strain engineered to contain a tet-off-*NCP1* allele

1416 (light green), and the same strain grown in the presence of doxycycline (orange). Growth in rich

1417 media, 1 µg/mL FLC, and 256 µg/mL FLC are shown.

1418

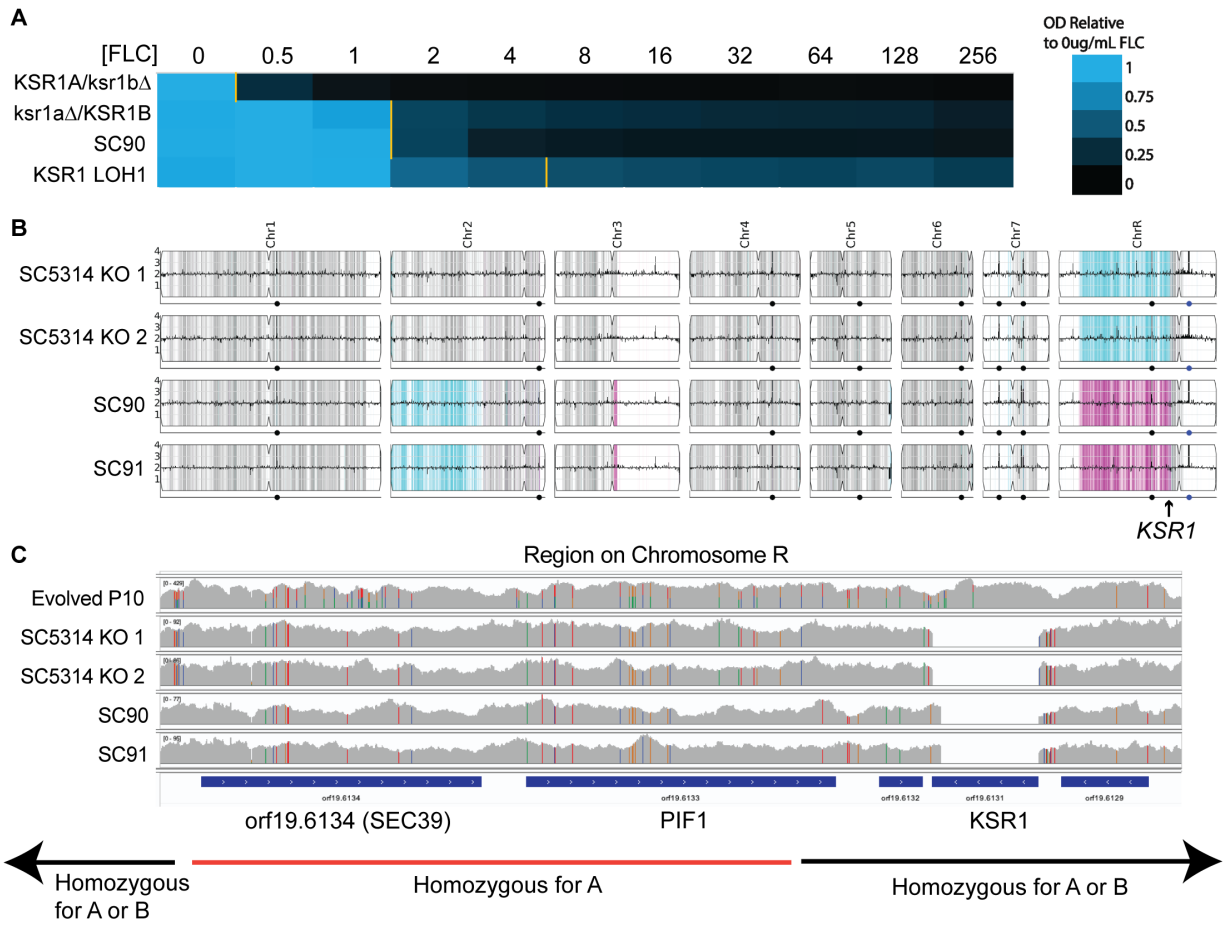

Fig S6. Heterozygous and homozygous deletion mutants of *KSR1*

(A) A heatmap showing OD_{600} values relative to growth in rich media after 24 hours in a broth microdilution assay for engineered strains with homozygous or heterozygous deletions of *KSR1*. The engineered strain containing the same *KSR1* genotype that evolved in *KSR1* LOH1 is shown last for comparison. Yellow lines indicate the FLC MIC_{50}. (B) Read depth from whole genome sequencing normalized to average depth across the whole genome is shown for 4 single colonies with complete deletions of *KSR1.* Colors indicate changes in allele frequencies at heterozygous positions. Blue indicates an increase in the proportion of the “A” reference allele, while pink indicates an increase in the proportion of the “B” reference allele, signifying losses of heterozygosity. (C) Read depth and SNV composition from integrated genomics viewer (IGV) are shown for one evolved isolate (Evolved P10) and engineered homozygous

knockout mutants in SC5314 and in BWP17 backgrounds. All four full knockout mutants show losses of heterozygosity, indicated by full color SNVs, including *orf19.6134* and *PIF1* which are all homozygous for the reference “A” allele. *KSR1* is flanked by the uncharacterized *orf19.6123* and *MRLP8*.

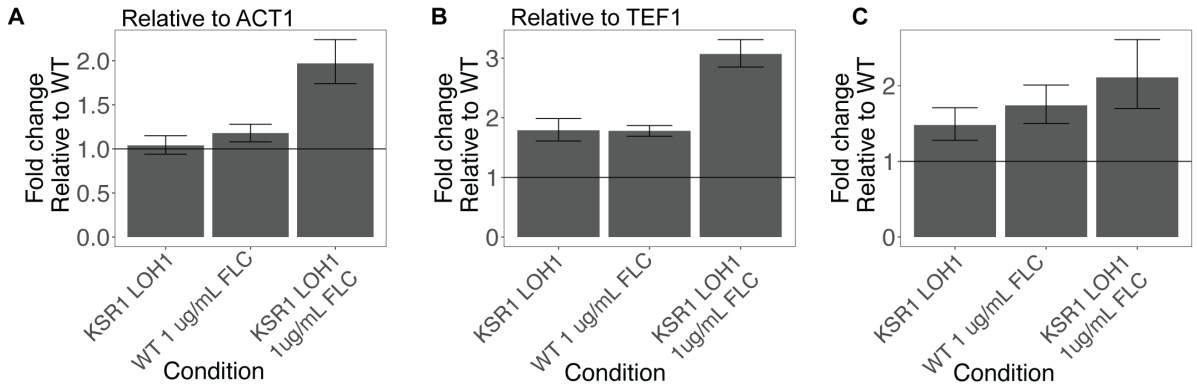

Fig S7. RT-qPCR for *CDR1* in *KSR1* LOH1 strain. (A) RT-qPCR data for one biological replicate in technical triplicate is shown for expression of the gene *CDR1* relative to the gene *ACT1* for the *KSR1* LOH1 engineered strain, the *KSR1* LOH1 engineered strain growth in 1 µg/mL FLC, and the progenitor strains grown in 1 µg/mL FLC, all relative to the WT (progenitor) strain grown in rich media. Error bars are standard deviations for technical triplicate with propagation of error during delta-delta CT calculations. (B) Data for the first biological replicate, calculated as in (A) but normalized to the gene *TEF1* rather than *ACT1*. (C) As in (A), RT-qPCR data for a second biological replicate in technical triplicate.

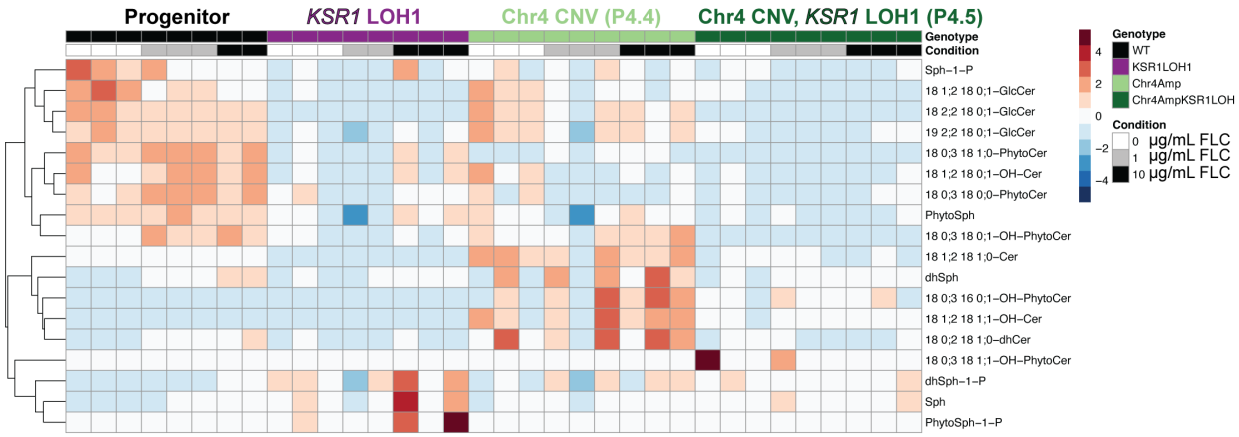

Fig S8. Lipid analysis of Chr4 CNV and *KSR1* LOH combinations. A heatmap showing levels of sphingolipid species present in each strain and condition relative to the mean of all samples for that lipid species. Heatmap colors indicate row-wise z-scores, blue being low and red being high. Rows are lipid species and columns are individual samples. Rows are clustered by k-means clustering as shown by the dendrogram on the left. Columns include 3 replicates each of the wild type progenitor strain (black) grown in 0 µg/mL (white), 1 µg/mL (grey), or 10 µg/mL FLC (black), the *KSR1* LOH1 engineered strain (purple), the single colony isolated from P4 that contained the Chr4 CNV alone (P4.4, light green), and the single colony from P4 that contained both the Chr4 CNV and *KSR1* LOH (P4.5, dark green) in the same conditions. Two outlier samples were removed (WT in 10 µg/mL FLC and *KSR1* LOH1 in 1 µg/mL FLC).

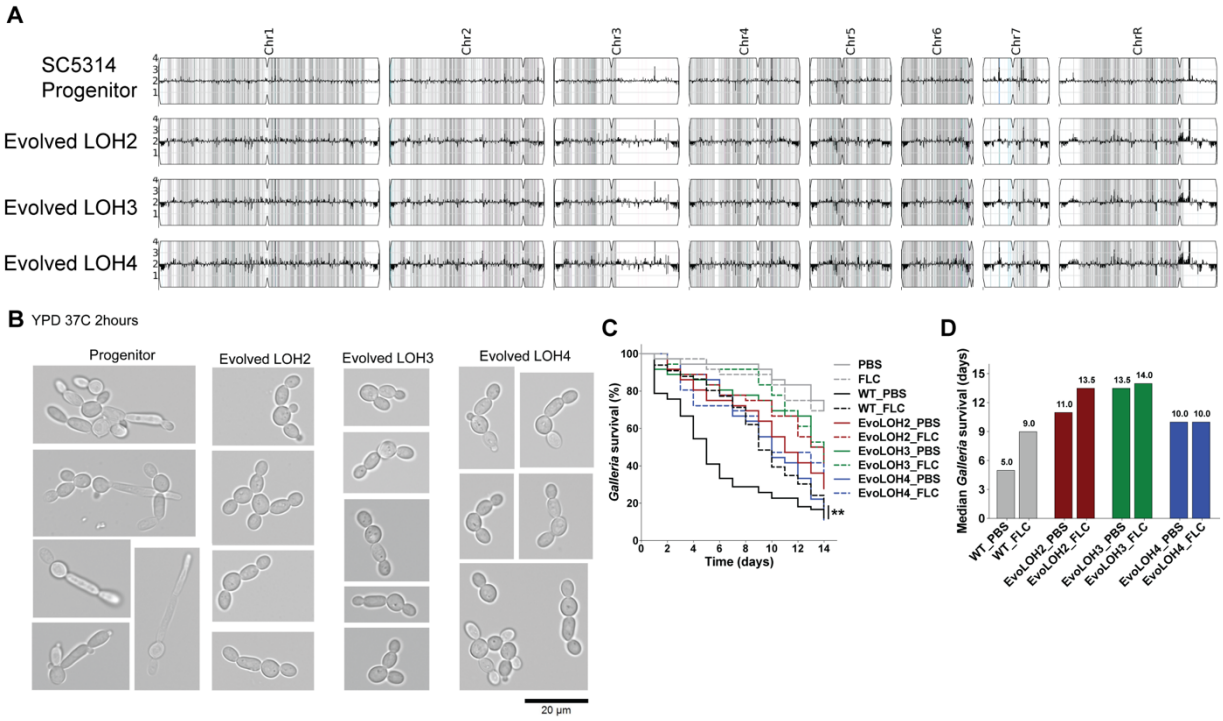

Fig S9. Additional evolved strains with LOH at *KSR1*. (A) Read depth from whole genome sequencing normalized to average depth across the whole genome for three evolved strains that all contain LOH at the *KSR1* locus and their SC5314 progenitor. Gray bars show heterozygous positions. (B) Microscopy of progenitor and evolved strains grown at 37℃ for 2 hours shows differences in the initiation of hyphal growth. (C) Survival curves for *G. mellonella* show a reduction in virulence for all three evolved strains relative to the progenitor (Log-rank test, ** $P < 0.01$). (D) Median *G. mellonella* survival over 14 days demonstrates that treatment with FLC increases survival of the wild-type strain (gray) but does not increase survival for larvae infected with evolved strains LOH3 (green) and LOH4 (blue).

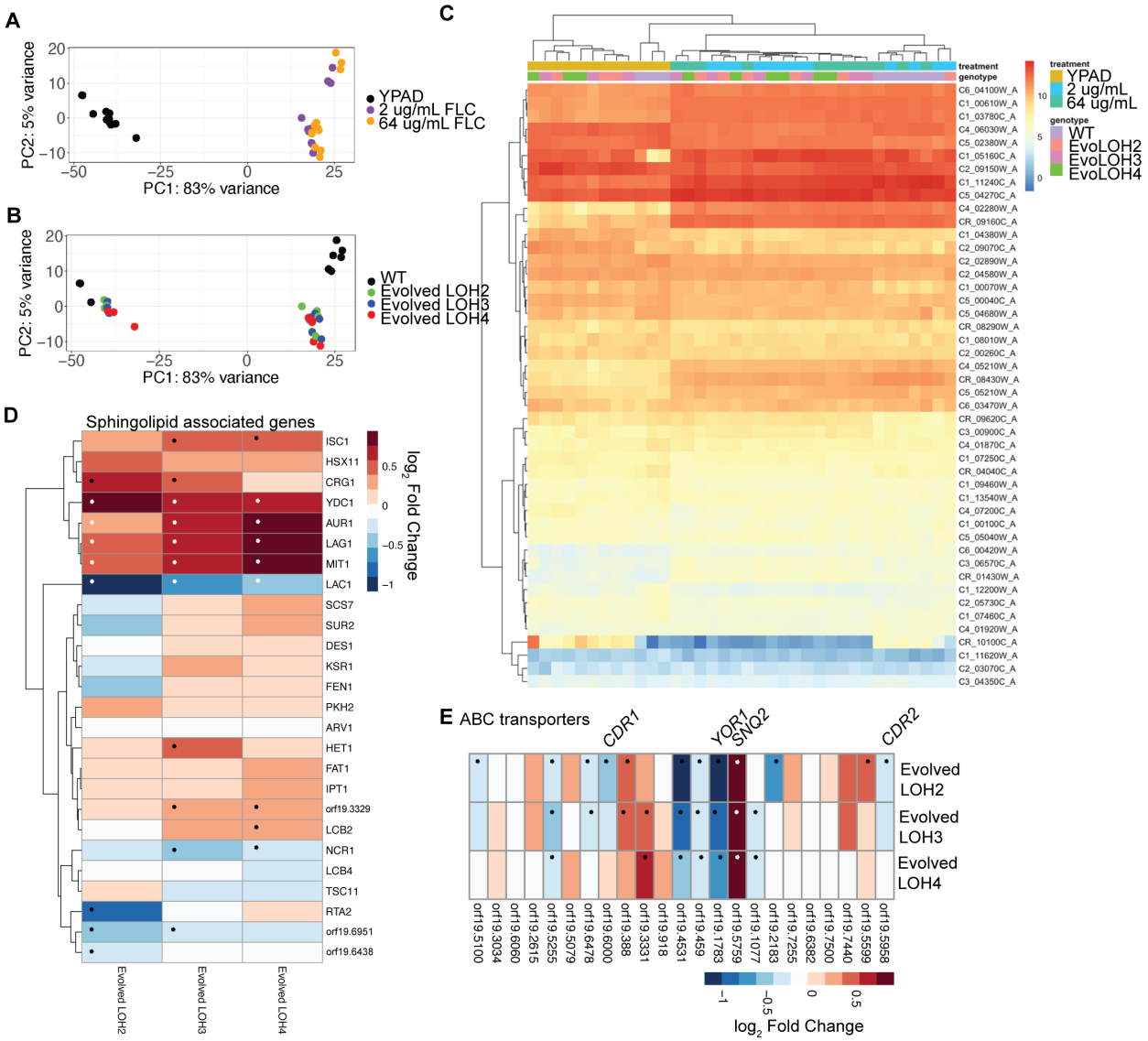

1469

1470 **Fig S10. RNA-sequencing analysis for Evolved LOH2, 3, and 4 isolates.** (A) Principal

1471 component analysis for RNA-sequencing data colored according to environmental condition. (B)

1472 Principal component analysis for RNA-sequencing data colored according to strain identity. (C)

1473 A heatmap showing normalized abundance from triplicate RNA-seq data for genes annotated as

1474 being related to sphingolipid biosynthesis. Rows are genes and columns are all samples,

1475 including the wild type progenitor, Evolved LOH2, Evolved LOH3, and Evolved LOH4 in the

1476 absence of FLC (YPD), 2 µg/mL FLC, or 64 µg/mL FLC. Row and column dendrograms from k-

1477 means clustering are shown on the top and left. (D) A heatmap shows the $\log_2$ fold changes

from triplicate RNA-seq data for genes catalyzing the steps of the sphingolipid biosynthesis pathway (Fig S1). Columns are strains Evolved LOH2, Evolved LOH3, and Evolved LOH4 relative to the wild type progenitor in 0 μg/mL FLC, and rows are genes annotated as part of the sphingolipid biosynthesis pathway or related to sphingolipid transport. Fold changes that are significantly different at an adjusted p-value of 0.1 are indicated with an asterisk. (E) As in (D), a heatmap shows $\log_2$ fold changes from triplicate RNA-seq data for genes annotated as ABC transporters.

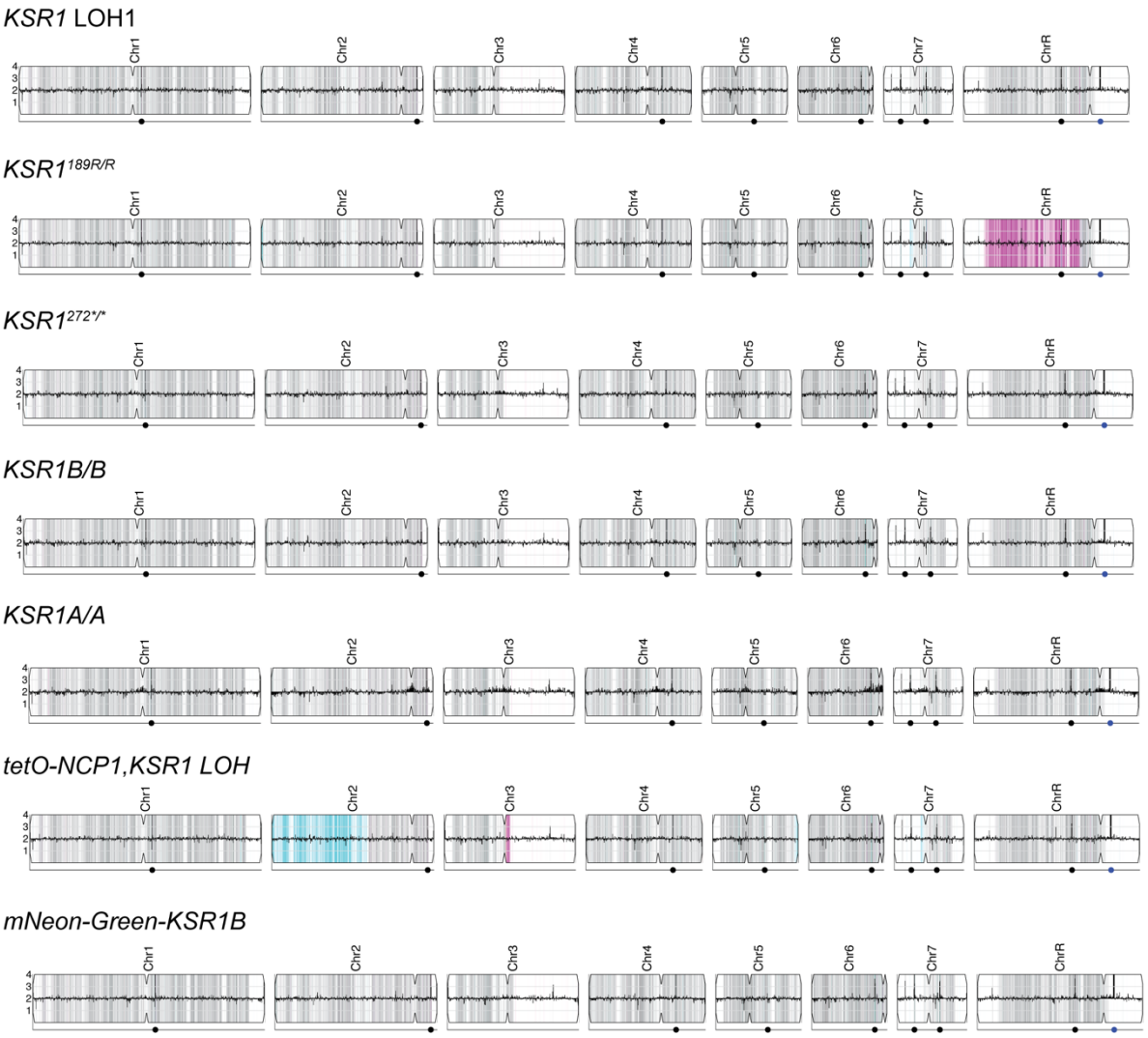

Fig S11. Whole Genome Sequencing for all engineered *KSR1* strains. For each *KSR1* mutant engineered strain, read depth is plotted on the y-axis according to genomic position on the x-axis. All strains shown are euploid (copy number of 2). In addition, grey bars show regions of heterozygosity, pink bars show regions of homozygosity of the "B" allele, and blue bars show homozygosity of the "A" allele. The *tetO-NCP1, KSR1* LOH1 strain was engineered in the SN152 genetic background, that includes LOH on Chr2 and a small region of Chr3. Points below each diagram mark the position of major repeat sequences.

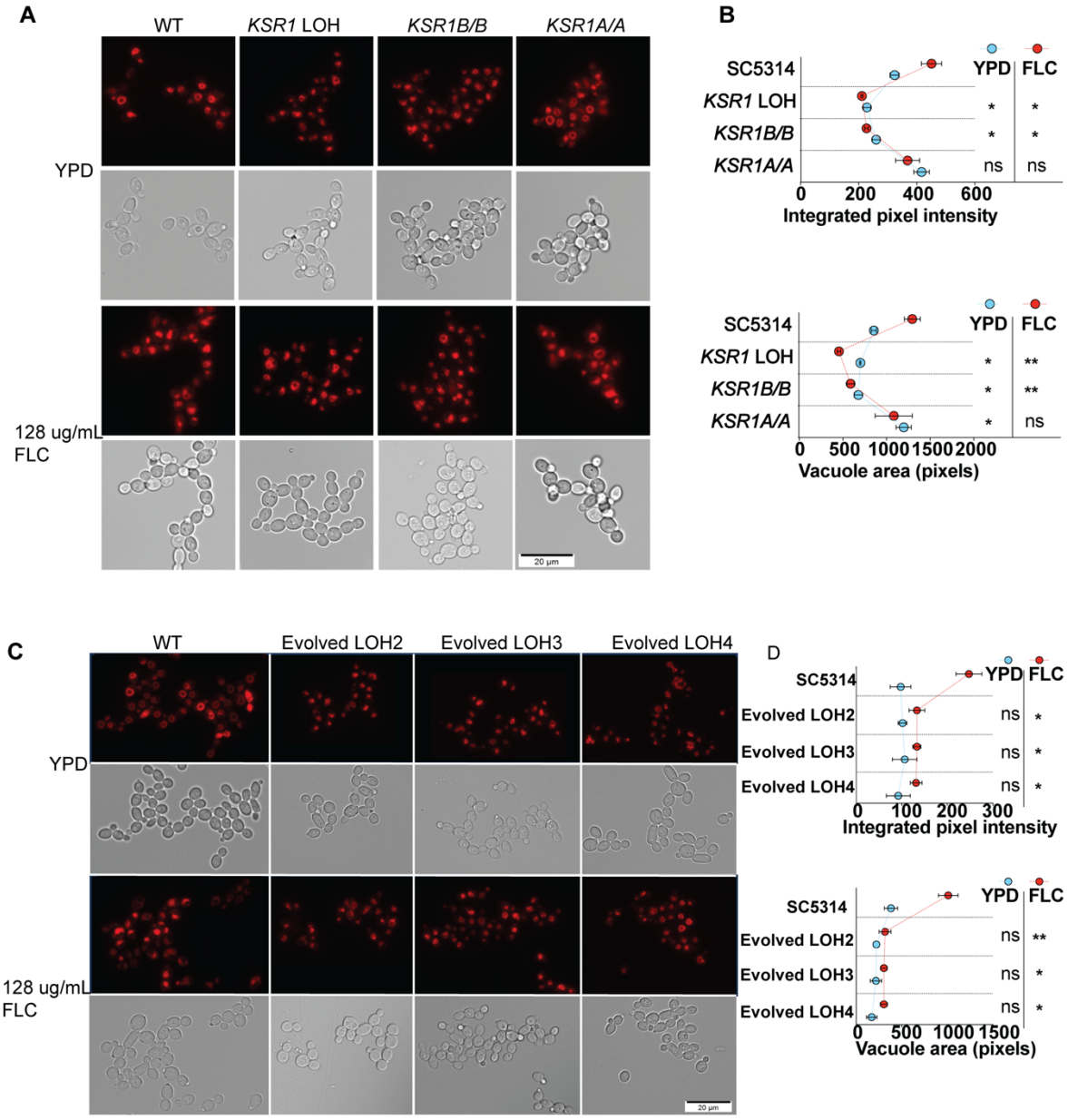

1495

1496 **Fig S12. Vacuolar phenotypes for evolved and engineered *KSR1* LOH mutants.** (A)

1497 Fluorescent microscopy (top rows) and DIC (subsequent rows) images for strains engineered to

1498 contain the *KSR1* LOH1 or to be completely homozygous for *KSR1* for either the A or B alleles.

1499 Cells were stained with the vacuolar dye FM4-64 after growth in YPD without drug (top) or after

1500 exposure to 128 µg/mL FLC (bottom). (B) Quantification of vacuolar area and integrated pixel

1501 intensity for fluorescence microscopy images shown in panel A, (see Methods). Points show an

1502 average of at least 200 cells and error bars represent standard errors of the mean (SEM). (C)
1503 As in A, fluorescence microscopy images of the additional three evolved strains with LOH
1504 affecting *KSR1*. (D) Quantification of fluorescence microscopy shown in panel (C). (B and D)
1505 Asterisks denote significant differences, using nonparametric t-tests, * $P < 0.05$, ** $P < 0.01$.
1506

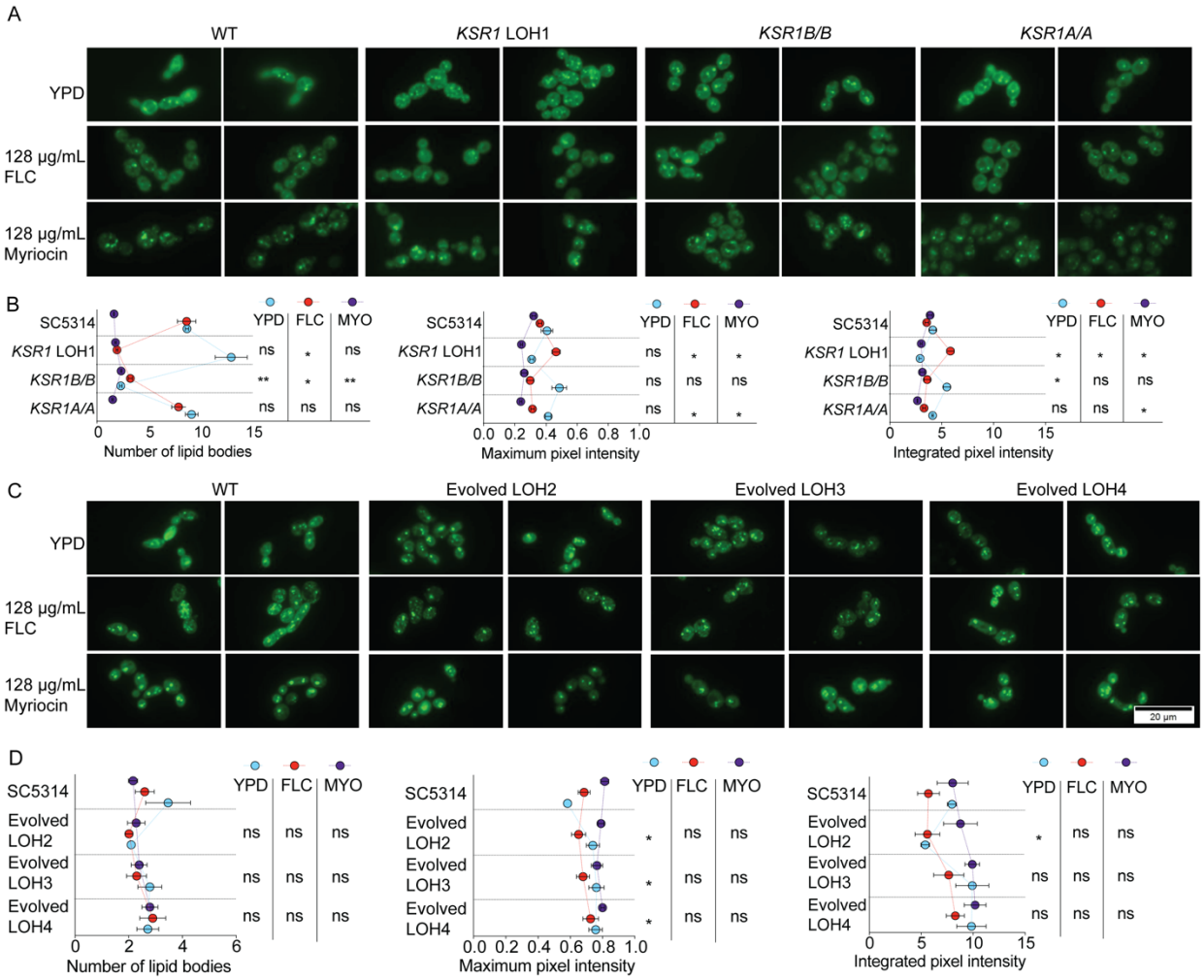

Fig S13. BODIPY staining and microscopy for evolved and engineered *KSR1* mutants. (A) Fluorescent microscopy images for cells from strains engineered to contain the *KSR1* LOH1 and to be completely homozygous for *KSR1* for either the A or B allele. Cells were stained with the lipid droplet dye BODIPY after growth in YPD alone (top), after exposure to 128 µg/mL FLC (middle), or after exposure to 128 µg/mL myriocin (MYO, bottom). (B) Quantification of the number of lipid droplets, lipid size, and integrated pixel intensity for fluorescence microscopy images, a subset of which are shown in panel (A), (see Methods). Points are an average of at least 200 cells and error bars represent standard errors of the mean (SEM). (C) As in A, fluorescence microscopy images for the three additional evolved strains with LOH affecting *KSR1*. (D) Quantification of fluorescence microscopy, a subset of which is shown in panel (C).

(B and D) Asterisks denote significant differences, using nonparametric t-tests, * P < 0.05, ** P < 0.01.

Table S1. Strains used in this study.

Table S2. Plasmids and oligos used in this study.